Sperm-specific COX6B2 enhances oxidative phosphorylation, proliferation, and survival in lung adenocarcinoma

Chun-Chun Cheng[1], Joshua Wooten[2], Zane Gibbs[1], Kathleen McGlynn[1], Prashant Mishra[3], Angelique W. Whitehurst[1]*

[1]Department of Pharmacology, Simmons Comprehensive Cancer Center, UT Southwestern Medical Center, 5323 Harry Hines Blvd Dallas, Texas 75390-8807, USA.
[2]Nuventra, 3217 Appling Way, Durham, NC 27703, USA
[3]Children's Research Institute, UT Southwestern Medical Center, Dallas, TX 75390, USA.

*Correspondence: Angelique.Whitehurst@UTSouthwestern.edu, 214-645-6066 (p), 214-645-6347 (f)

ABSTRACT

Cancer testis antigens (CTAs) are genes whose expression is normally restricted to the testis but anomalously activated in cancer. In sperm, a number of CTAs promote energy generation, however whether these proteins contribute to tumor cell metabolism is not understood. Here we describe COX6B2, a sperm-specific component of cytochrome c oxidase (complex IV). COX6B2 is frequently expressed in human lung adenocarcinoma (LUAD) and expression correlates with reduced survival time in patients. COX6B2, but not its somatic isoform COX6B1, enhances activity of complex IV, increasing mitochondrial oxidative phosphorylation (OXPHOS) and NAD^+ generation. Consequently, COX6B2-expressing cells display a proliferative advantage, particularly in low oxygen conditions. Conversely, depletion of COX6B2 attenuates OXPHOS and collapses mitochondrial membrane potential leading to cell death or senescence.

29 Furthermore, COX6B2 is both necessary and sufficient for growth of tumors *in vivo*. Our
30 findings reveal a previously unappreciated, tumor specific metabolic pathway hijacked
31 from one of the most ATP-intensive processes in the animal kingdom: sperm motility.

32

33 **INTRODUCTION**

34 Tumors frequently activate genes whose expression is otherwise restricted to testis; these
35 genes are known collectively as cancer-testis antigens (CT-antigens, CTAs). The
36 expression of these genes outside their native and immune privileged site has been the
37 basis for immunotherapeutic approaches including vaccines and adoptive T-cell therapy
38 (Hunder et al. 2008; Gjerstorff, Andersen, and Ditzel 2015). Historically, functional
39 knowledge of the contribution of these proteins, if any, to neoplastic behaviors has
40 significantly lagged behind immune-targeting. In recent years, the functional
41 characterization of CTAs has gained broader interest and these proteins have been
42 implicated in tumor cell survival, TGF-β signaling, mitotic fidelity, polyadenylation, mRNA
43 export, tumor suppressor silencing, and DNA damage repair (Gibbs and Whitehurst 2018;
44 Viphakone et al. 2015; Nichols et al. 2018). Multiple reports now indicate that anomalous
45 expression of testis proteins can be engaged to support the tumorigenic program. The
46 biased expression pattern of these proteins to tumors and testis may offer an
47 extraordinarily broad therapeutic window if they can be targeted directly.

48 One unique aspect of mammalian sperm physiology is the tremendous energy demand
49 required for motility while preserving the integrity of their precious DNA cargo within the
50 hostile environment of the female reproductive tract. To meet this demand, sperm contain
51 a number of tissue specific protein isoforms for glycolysis and oxidative phosphorylation
52 (OXPHOS) that mediate the increase in ATP production. For example, lactate

53 dehydrogenase C, LDHC, is a testis-specific isoform of the terminal enzyme in glycolysis
54 that catalyzes the reduction of pyruvate to lactate essential for male fertility (Odet et al.
55 2008; Krisfalusi et al. 2006; Li et al. 1989). Similarly, COX6B2 is a testis-specific subunit
56 of cytochrome c oxidase (complex IV) (Huttemann, Jaradat, and Grossman 2003). mRNA
57 encoding of either LDHC or COX6B2 is undetectable in normal tissue, but both are
58 upregulated in a number of different tumor derived cell lines, classifying them as CTAs
59 ((Maxfield et al. 2015), (CTpedia (http://www.cta.lncc.br/index.php)). However, it is
60 unclear whether these proteins support metabolic programs in tumor cells.
61 In a large-scale loss of function analysis to annotate the contribution of individual CTAs
62 to neoplastic behaviors, we found that COX6B2 is essential for survival of non-small cell
63 lung cancer (NSCLC) cell lines (Maxfield et al. 2015). COX6B2 is a nuclear encoded,
64 sperm-specific component of complex IV (Huttemann, Jaradat, and Grossman 2003). By
65 transferring electrons from reduced cytochrome c to O_2, complex IV is the rate-limiting
66 step for ATP production by the electron transport chain (ETC). Thirteen subunits make
67 up complex IV: three are mitochondrial encoded and ten are derived from nuclear DNA.
68 Six of the ten nuclear encoded subunits have tissue-specific isoforms that permit
69 regulation of this complex in response to environmental cues (e.g. pH, hormones, metals,
70 ATP/ADP ratio etc.) (Kadenbach and Huttemann 2015). The somatic isoform of COX6B2
71 is COX6B1. These two proteins share 58% amino acid identity and ~80% similarity.
72 Based on structural information, it is apparent that COX6B1/2 are the only complex IV
73 subunits that are not membrane bound. Instead, their localization is confined to the
74 intermembrane space where cytochrome c associates. It is inferred that COX6B1/B2
75 participate in dimerization of complex IV and cytochrome c association (Sampson and

76 Alleyne 2001; Tsukihara et al. 1996). While limited, studies on COX6B1 indicate that it is
77 essential for complex IV activity. In particular, human mutations in COX6B1 (R20C or
78 R20H) abrogate complex IV assembly and lead to severe cardiac defects (Abdulhag et
79 al. 2015). In addition, biochemical analysis indicates that removal of COX6B1 from
80 assembled complexes enhances complex IV activity, implying a negative regulatory role
81 for COX6B1 (Weishaupt and Kadenbach 1992). To-date no reports detail the function of
82 COX6B2 nor indicate the physiological relevance of this sperm-specific subunit to fertility.
83 Furthermore, there are no reports describing mechanism(s) that regulate COX6B1 or
84 COX6B2 expression. Overall, compared to the enormous data on complex IV in general,
85 the COX6B proteins have been understudied.
86 We have undertaken a detailed investigation into the mechanism of action of COX6B2
87 when this protein is aberrantly expressed in NSCLC. Here, we report that COX6B2
88 enhances mitochondrial oxidative phosphorylation (OXPHOS) in tumor cells. This activity
89 accelerates proliferation *in vitro* and *in vivo*. In contrast, silencing of COX6B2 attenuates
90 OXPHOS, reduces tumor cell viability and dramatically decreases growth *in vivo*.
91 Importantly, we find that hypoxia enhances COX6B2 expression, which confers a
92 selective advantage for proliferation under low oxygen. Indeed, elevated COX6B2 mRNA
93 correlates with reduced survival of LUAD patients. Cumulatively, this study demonstrates
94 the remarkable capacity of tumor cells to integrate primordial gene products into their
95 regulatory environment as a means of promoting unrestrained proliferation. In turn,
96 COX6B2 becomes a liability that may be exploited for tumor selective targeting of
97 OXPHOS.
98

99 **RESULTS**

100 **COX6B2 is expressed in lung adenocarcinoma (LUAD) tumors and correlates with**
101 **poor survival**

102 Using a large-scale functional genomics approaches, we previously found that depletion
103 of COX6B2 activates cleaved caspase 3/7 in cell lines derived from breast, melanoma
104 and NSCLC, with the most potent activation in H1299 NSCLC cells **(Figure 1-figure**
105 **supplement 1A)** (Maxfield et al. 2015)**.** Based on these findings, we examined the
106 relationship between COX6B2 expression and patient outcome in NSCLC. Strikingly,
107 elevated expression of COX6B2 is associated with significantly shorter overall survival
108 (OS) time (P = 5.3 x10^{-6}, log rank test; hazard ratio (HR): 1.46; 95% confidence interval
109 (CI): 1.24-1.73) **(Figure 1A)**. In addition, COX6B2 expression positively correlates with
110 time to first progression (FP) (P = 4.1 x10^{-4}, log rank test; HR: 1.63; 95% CI: 1.24-2.14)
111 **(Figure 1A)**. Separation of the two major histological subtypes of NSCLC revealed a
112 strong correlation for both outcomes in LUAD (OS: P = 1.6 x10^{-4}, log rank test; HR: 1.59;
113 95% CI: 1.25-2.03; FP: P = 9.4 x10^{-5}, log rank test; HR: 1.91; 95% CI: 1.37-2.65) **(Figure**
114 **1B)**. However, this correlation is not observed in lung squamous carcinoma (LUSC) (OS:
115 P = 0.75, log rank test; HR: 1.05; 95% CI: 0.77-1.44; FP: P = 0.96, log rank test; HR: 0.99;
116 95% CI: 0.59-1.65) **(Figure 1C)**. Analysis of TCGA data sets also revealed a significant
117 upregulation of COX6B2 mRNA in LUAD tumors as compared to normal tissues **(Figure**
118 **1D)**. We next immunoblotted for COX6B2 protein in a panel of LUAD tumors and normal
119 lung tissue using an antibody that detects COX6B2 **(Figure 1E; figure 1-figure**
120 **supplement 1B)**. We found that COX6B2 protein expression is low or undetectable in
121 normal lung tissue, but present in all tumor-derived tissues irrespective of stage and grade

122 **(Figure 1E; Figure 1-figure supplement 1C)**. A similar pattern is also observed in LUAD-
123 derived cell lines **(Figure 1F)**. Furthermore, immunohistochemical staining of COX6B2 in
124 a panel of non-malignant (n = 22) and LUAD tissues (n = 32) indicated accumulation of
125 COX6B2 in tumor, but not non-malignant tissues **(Figure 1G)**. This expression of
126 COX6B2 in tumors does not have an apparent correlation with the presence or absence
127 of COX6B1, the somatic isoform of COX6B2. We did observe a moderate correlation with
128 the complex IV subunit, COXIV, suggesting COX6B2 accumulation coincides with
129 increased mitochondria in cancer cells **(Figure 1-figure supplement 1D)**. Furthermore,
130 depletion or overexpression of either COX6B1 or COX6B2 does not impact protein
131 accumulation of the corresponding isoform **(Figure 1-figure supplement 1B)**. These
132 findings indicate that while the isoforms are closely related in sequence their regulation
133 may be through independent mechanisms. Immunofluorescence of endogenous
134 COX6B2 in intact LUAD cells revealed specific localization to the mitochondria as judged
135 by overlap with Tom20, a mitochondrial resident protein **(Figure 1H)**. Thus, COX6B2 is
136 frequently expressed in LUAD, correlates with poor survival and when ectopically
137 expressed can localize to its native mitochondrial location.
138

139 **COX6B2, but not COX6B1, enhances oxidative phosphorylation in LUAD**

140 To investigate whether COX6B2 supports OXPHOS when ectopically expressed in
141 tumors, we generated a LUAD cell line that overexpresses COX6B2 protein ~3-fold
142 (HCC515-COX6B2-V5) **(Figure 2A)**. This overexpression is not associated with an
143 increase in mitochondrial DNA or total mitochondria **(Figure 2B-C)**. We then measured
144 the oxygen consumption rate (OCR) at baseline and following exposure to electron

145 transport chain perturbagens. This analysis revealed a significant enhancement in basal,
146 ATP-linked, maximal and reserve OCR in COX6B2-V5 expressing cells as compared to
147 control **(Figure 2D)**. A similar trend is observed in an independent LUAD cell line, H2122,
148 expressing COX6B2-V5 **(Figure 2E-F)**. The OCR increase is associated with an elevation
149 in total ATP in both cell lines **(Figure 2G)**. In addition, we observed elevated NAD^+/NADH
150 in COX6B2-V5 cells, indicative of an overall increase in electron transport activity **(Figure**
151 **2H)**. We did not observe a significant or reproducible alteration in extracellular
152 acidification rate (ECAR) in either setting **(Figure 2I)**. We also studied whether COX6B2's
153 somatic isoform, COX6B1, was sufficient to enhance OCR **(Figure 2J)**. COX6B1-V5
154 expression appears to have no effect or slightly decreases OCR for each parameter
155 **(Figure 2K)**, consistent with prior biochemical studies where COX6B1 removal enhances
156 the activity of complex IV (Weishaupt and Kadenbach 1992).
157

158 **COX6B2 enhances complex IV activity and is incorporated into mitochondrial**
159 **supercomplexes**

160 To further characterize the impact of COX6B2 on complex IV, we directly assessed
161 complex IV activity using a technique to pharmacologically isolate complex IV in
162 permeabilized COX6B1-V5 or COX6B2-V5 cells (Salabei, Gibb, and Hill 2014;
163 Divakaruni, Rogers, and Murphy 2014) **(Figure 3A)**. Here, we find that COX6B2-V5
164 overexpression confers a significant increase (~25%) in complex IV activity in both
165 LUAD cell lines tested **(Figure 3B)**. In contrast, a minimal, statistically insignificant
166 increase in activity was observed following COX6B1-V5 overexpression **(Figure 3C)**.
167 The increase in complex IV activity did not correlate with any apparent increase in the

168 abundance of complex IV as judged by COXIV accumulation (**Figure 3- figure**
169 **supplement 1A)**. This finding suggests that COX6B2 is a rate limiting subunit of
170 complex IV.

171 Recently, a number of reports have suggested that tissue specific complex IV
172 isoforms may promote supercomplex formation and selectively and specifically increase
173 ATP production in tumor cells (Maranzana et al. 2013; Ikeda et al. 2019).
174 Supercomplexes contain multiple electron transport sub-complexes containing complex
175 III and IV and are hypothesized to promote local channeling of substrates, trapping of
176 reactive intermediates and/or subunit stabilization (Acin-Perez et al. 2008). To test this
177 possibility for COX6B2, we used Blue-native PAGE (BN-PAGE) analysis to separate
178 electron transport chain complexes (monomers (IV) and dimers (IV_2) and
179 supercomplexes (III_2+IV and I+III_2+IV_n) in control and COX6B1/B2-V5 expressing cells.
180 Here, we observed that >90% of endogenous COX6B2 is found in in complex IV dimers
181 or incorporated into supercomplexes. In contrast, >98% COX6B1 is found in monomeric
182 complex IV **(Figure 3D-E; Figure 3-figure supplement 1B)**. This trend is maintained
183 when either isoform is overexpressed (>85% of COX6B2 is in complex IV in
184 dimers/supercomplexes versus 40% for COX6B1) **(Figure 3F)**.

185 We next tested the polymeric distribution of complex IV, using analysis of COXIV,
186 a core protein subunit of complex IV, following COX6B1-V5 or COX6B2-V5 expression.
187 Here, we found that upon expression of COX6B2-V5, but not COX6B1-V5, the
188 distribution of complex IV shifted from monomers to increased formation of
189 supercomplexes **(Figure 3G)**. Supercomplexes are hypothesized to enhance electron
190 transport activity without a compensatory increase in ROS (Maranzana et al. 2013).

191 Indeed, COX6B2 overexpressing cells do not display a concomitant induction of
192 superoxide **(Figure 3H)**. These data indicate that COX6B2 preferentially integrates into
193 dimeric complex IV and supercomplexes, and enhanced COX6B2 expression promotes
194 incorporation of complex IV into supercomplexes. These alterations in distribution are
195 proposed to enhance mitochondrial OXPHOS while limiting oxidative stress.
196

197 **COX6B2 enhances cell proliferation and confers a growth advantage in low**
198 **oxygen**

199 We next investigated whether the expression of COX6B2 is sufficient to enhance the
200 growth of LUAD cells. We observed an increase in DNA synthesis as measured by EdU
201 incorporation of 50.39 ± 6.35% in HCC515 and 38.7 ± 8.4% in H2122 **(Figure 4A; figure**
202 **4-figure supplement 1A)**. Notably, an increase is not observed for COX6B1-V5
203 overexpression consistent with no significant change in OCR **(Figure 4A,** middle panel**;**
204 **Figure 2K)**. In addition, we observed an enhanced population double rate of 37.16 ±
205 10.71% and 29.88 ± 6.74% for the HCC515 and H2122 cells, respectively **(Figure 4B** (-)
206 Pyruvate column; compare red and blue bars; **Figure 4-figure supplement 1B)**.
207 Mitochondrial OXPHOS has been linked to proliferation via regulation of the NAD^+/NADH
208 ratio, which is elevated in COX6B2-V5 overexpressing cells **(Figure 2H)** (Birsoy et al.
209 2015; Sullivan et al. 2015). Consistent with this model, supplementation with pyruvate, an
210 electron acceptor which drives NAD^+ production, largely diminishes the proliferative
211 effects of COX6B2-V5 overexpression **(Figure 4B)**. A similar proliferative advantage is
212 also observed when COX6B2-V5 cells are grown in the absence of extracellular matrix,
213 suggesting that COX6B2 promotes anchorage-independent growth **(Figure 4C)**.

214 Isoforms of complex IV subunits can be selectively expressed to permit adaptation to
215 tissue-specific needs or environmental conditions (Sinkler et al. 2017). In particular,
216 hypoxia is reported to regulate complex IV subunit expression and permit continued
217 respiration in low oxygen (Ikeda et al. 2019; Hayashi et al. 2015; Fukuda et al. 2007).
218 Therefore, we cultured control and COX6B2-V5 overexpressing cells in low (2.5%) O_2 for
219 four days, monitoring EdU incorporation every 24 hours. Under these conditions, control
220 cells reduce EdU incorporation by ~60%, while COX6B2-V5 expressing cells decrease
221 incorporation by 15% **(Figure 4D; figure 4- figure supplement 1C)**. This data indicates
222 that COX6B2 expression can enhance proliferation in both normoxia and low oxygen
223 conditions. Given this phenotype, we examined whether COX6B2 is regulated in
224 response to low oxygen. ChIP data from human breast cancer cells indicates that HIF-1
225 is bound near the COX6B2 promoter (Zhang et al. 2015). In addition, we also identified
226 11 putative HREs (A/G-CGTG) which are enriched at the HIF-1 peaks **(Figure 4-figure**
227 **supplement 1D)**. Indeed, we observed a greater than two-fold increase in COX6B2 but
228 not COX6B1 mRNA following 12 hours of 2.5% oxygen **(Figure 4E)**. This accumulation
229 of mRNA was associated with stabilization of COX6B2 protein **(Figure 4F)**. Under both
230 normoxic or hypoxic conditions, we did not observe any significant alteration in COX6B2
231 or COX6B1 accumulation when the alternative isoform was overexpressed, indicating that
232 the changes in expression are not an isoform switch **(Figure 1-figure supplement 1B;**
233 **Figure 4-figure supplement 1E)**. Collectively, these data suggest that the enhanced
234 electron transport activity in COX6B2 expressing cells confers a selective advantage by
235 promoting key tumorigenic behaviors including unrestrained proliferation, anchorage
236 independent growth and enhanced survival in hypoxia.

237

238 **Depletion of COX6B2 impairs mitochondrial electron transport chain function in**
239 **LUAD cells**

240 Given the pro-proliferative phenotype following COX6B2 expression, we next examined
241 the consequences of its depletion on OXPHOS and tumor cell viability. Reduction of
242 COX6B2 protein using shRNA pools (four independent sequences) or siRNA pools (two
243 independent sequences), led to a decrease in basal, ATP-linked, maximal and reserve
244 OCR in HCC515 and H2122 cell lines **(Figure 5A-B; figure 5-figure supplement 1A)**.
245 We were unable to establish a stable clone of COX6B2 deleted cells by CRISPR/Cas9.
246 However, COX6B2 directed CRISPR/Cas9 did generate a population with reduced
247 COX6B2 protein expression **(Figure 5-figure supplement 1B)**. In agreement with the si
248 and shCOX6B2 data, sgCOX6B2 cells also exhibit attenuated OCR **(Figure 5-figure**
249 **supplement 1C)**. The reduction in OCR following COX6B2 depletion is accompanied by
250 a reduction in the NAD^+/NADH ratio **(Figure 5C)**. In addition, total cellular ATP is
251 decreased following siRNA-mediated COX6B2 depletion with two independent siRNA
252 sequences across a panel of COX6B2-expressing LUAD cell lines **(Figure 5D)**.
253 Consistent with a loss of electron transport chain function, depletion of COX6B2 resulted
254 in decreased mitochondrial membrane potential **(Figure 5E)** and increased intracellular
255 hydrogen peroxide **(Figure 5F)**. Collectively, these findings indicate that COX6B2 is
256 essential for respiration and mitochondrial integrity in tumor cells.

257

258 **Depletion of COX6B2 decreases cell survival and induces cell apoptosis and**
259 **senescence**

260 Based on the observed decrease in OCR, we asked whether tumor cell viability was
261 diminished following COX6B2 depletion in LUAD cells. Depletion of COX6B2 for nine
262 days, results in a decrease in EdU incorporation **(Figure 6A)**. Furthermore, these cells
263 are severely compromised in their ability to grow in the absence of an extracellular matrix
264 **(Figure 6B)**. Both of these phenotypes were recapitulated in sgCOX6B2 cells (**Figure 6-**
265 **figure supplement 1A-B).** We next examined the underlying mechanism(s) leading to
266 the observed loss of viability. In our original screen, we found that siRNA-mediated
267 depletion of COX6B2 enhances cleavage of caspase 3/7, a phenotype that is rescued in
268 COX6B2-V5 overexpressing cells (**Figure 6C-figure supplement 1C)** (Maxfield et al.
269 2015). In cells where COX6B2 is depleted using a pool of shRNAs, with sequences
270 independent of the those in the siRNA pool, we observed cleavage of caspase-3 and
271 PARP **(Figure 6C)**. These cell death markers are also induced in sgCOX6B2 cells
272 (**Figure 6-figure supplement 1D)**. The induction of cell death proteins is accompanied
273 by an increase in Annexin-V staining, demonstrating activation of caspase-dependent
274 programmed cell death **(Figure 6D)**. Visual inspection of COX6B2 depleted cultures also
275 revealed a population of cells that are flattened, accumulate vacuoles, and in some cases,
276 are multi-nucleated, feature reminiscent of senescence **(Figure 6E)**. Staining of these
277 cells revealed an increase in β-galactosidase, suggesting induction of a cellular
278 senescence program **(Figure 6F)**. To determine the underlying trigger for the reduction
279 in survival, we attempted to rescue the death through multiple approaches.
280 Supplementing depleted cells with pyruvate and uridine as metabolic and nucleotide fuel
281 was insufficient to rescue the viability defects **(Figure 6-figure supplement 1E-F)**.
282 However, exposing cells to the ROS scavenger N-acetyl-l-cysteine (NAC) reduced the

283 extent of the cleaved caspase-3 and PARP and β-galactosidase staining **(Figure 6G-H).**
284 Thus, COX6B2 is essential for survival of LUAD tumor cells as its suppression reduces
285 ATP, compromises mitochondrial integrity thereby generating excess ROS that leads to
286 apoptosis or senescence.
287

288 **COX6B2 is necessary and sufficient for tumor growth *in vivo***

289 We next sought to determine whether COX6B2 was necessary and/or sufficient for
290 tumor growth *in vivo*. We implanted control and COX6B2-V5 HCC515 cells into the flank
291 of FOXn1^{nu} (nude) mice. Importantly, tumors engrafted subcutaneously encounter a
292 highly hypoxic environment (~0.08 – 0.8% O_2) (Helmlinger et al. 1997). In agreement
293 with the cell line data, we observed enhanced growth of COX6B2-V5 expressing cells *in*
294 *vivo* **(Figure 7A)**. After 38 days, COX6B2-V5 tumors exhibit a 4X greater mass than
295 control **(Figure 7B)**. In the converse experiment, we xenografted control and
296 shCOX6B2 cells in the flank of immunocompromised mice. Complementing the gain of
297 function phenotype observed, we found that depletion of COX6B2 severely reduces
298 tumor growth and final tumor mass **(Figure 7C-D)**. Taken together, our findings indicate
299 that the anomalous expression of COX6B2 is both necessary and sufficient for growth
300 of LUAD tumors.
301

302 **DISCUSSION**

303 COX6B2 function has remained obscure in both tumor cells and sperm since its
304 discovery (Huttemann, Jaradat, and Grossman 2003). Our data indicate that COX6B2
305 enhances complex IV activity leading to an increase in mitochondrial oxidative

306 phosphorylation. The function of COX6B2 appears to differ from COX6B1, which did not
307 enhance OXPHOS when overexpressed, a finding consistent with previous biochemical
308 analyses that indicate removal of COX6B1 enhances complex IV activity (Weishaupt and
309 Kadenbach 1992). Genetic studies demonstrate that human mutations in COX6B1 reduce
310 assembly of complex IV and other ETC complexes. Based on this cumulative data, we
311 hypothesize that COX6B1 (and perhaps B2) are essential for assembly and regulation of
312 complex IV. In normal tissues, COX6B1 may regulate complex IV to prevent the
313 generation of excessive and unused energy and also damaging ROS. In sperm, where
314 ATP demand is high, COX6B2 expression could promote complex IV dimerization and
315 incorporation into supercomplexes to promote efficient OXPHOS and limit ROS
316 production that would otherwise damage DNA (Agarwal et al. 2014). This function may
317 be particularly important during early tumorigenesis, where a highly hypoxic environment
318 can lead to proliferative arrest and excessive ROS generation. We propose that tumor
319 cells that express and engage the COX6B2-based, sperm-specific mechanism can
320 overcome this innate barrier to transformation that would otherwise restrict cell survival.
321 One of the most surprising aspects of our study was the loss of tumor cell viability
322 following the depletion of COX6B2. As COX6B2 enhances OXPHOS, its loss would be
323 expected to reduce ATP levels and the NAD^+/NADH ratio and slow proliferation, but not
324 necessarily kill tumor cells. Tumor cell glycolytic pathways should theoretically
325 compensate for reduced energy generation. Moreover, the presence of COX6B1 should
326 be able to support complex IV function. Instead, we observe ROS production and an
327 exit from the cell cycle either to death or senescence. This finding implies that these
328 cells are highly dependent upon OXPHOS for survival. In addition, the loss of COX6B2

329 may promote apoptosis due to a collapse of mitochondrial membrane potential and
330 cytochrome c egress (Smaili et al. 2001; Tai et al. 2017).
331 The majority of tumor metabolism studies have focused on the contribution of the
332 Warburg effect and have led to the notion that OXPHOS is dispensable for many
333 transformed cells. However, a growing body of evidence indicates that OXPHOS is
334 essential for tumor cell division and survival. First, OXPHOS contributes to >80% of total
335 ATP production in tumor cells, which is essential for satisfying the demands of
336 proliferation and tumor progression (Rao et al. 2019; Lissanu Deribe et al. 2018; Zu and
337 Guppy 2004). Second, OXPHOS provides electron acceptors to generate metabolic
338 intermediates (e.g. aspartate) that are required for continued cell division (Sullivan et al.
339 2015). Third, tumor cells exhibit enhanced sensitivity to inhibitors of OXPHOS (Nayak et
340 al. 2018; Scotland et al. 2013). Fourth, isoform switching of complex IV subunits is
341 observed in tumors and is associated with aggressive malignant behaviors (Oliva et al.
342 2015; Zhang et al. 2016; Minton et al. 2016). Finally, OXPHOS is upregulated and
343 essential for survival during ER-stress, hypoxia and glucose limiting conditions, and
344 exposure to targeted therapies (Balsa et al. 2019; Ikeda et al. 2019; Fukuda et al. 2007;
345 Guieze et al. 2019). Based on these and a vast array of additional data, it is accepted that
346 inhibition of OXPHOS is a tractable therapeutic entry point for treating cancer (Weinberg
347 and Chandel 2015). Indeed, extensive studies with metformin have demonstrated anti-
348 proliferative activities and reduction of tumor incidence through the inhibition of Complex
349 I (Weinberg and Chandel 2015). However, this and other ETC inhibitors cannot
350 discriminate between tumor or normal cells, limiting their therapeutic window. We propose
351 that enhanced accumulation of COX6B2 is an acquired trait that is essential for OXPHOS

352 in LUAD and perhaps additional cancers. At minimum, elevated COX6B2 protein
353 expression is a functional enrollment biomarker for OXPHOS inhibitor based treatment.
354 Moreover, COX6B2 structural elements that are distinct from COX6B1 could represent
355 targets for small molecule inhibitors. Finally, due to expression in an immune privileged
356 site, CTAs have long been considered ideal targets for immunotherapy. However, no
357 objective criterion exists to prioritize them for immunotherapy. We propose that COX6B2
358 represents an ideal candidate for immunotherapy because it has a bona fide tumorigenic
359 function. Specifically, sequence differences between COX6B2 and COX6B1 could permit
360 antigen recognition by patient immune cells and thus act as targets of adoptive T-cell
361 transfer.
362

363 **MATERIAL AND METHODS**

Key Resources Table				
Reagent type (species) or resource	**Designation**	**Source or reference**	**Identifiers**	**Additional information**
strain, strain background (*Mus musculus, female*)	Hsd:Athymic Nude-Foxn1^{nu}	Envigo		
cell line (*Homo sapiens*)	HEK293T	ATCC	CRL-3216; RRID:CVCL_0063	
cell line (*Homo sapiens*)	H1395	John Minna		UT Southwestern
cell line (*Homo sapiens*)	H1373	John Minna		UT Southwestern
cell line (*Homo sapiens*)	H2030	John Minna		UT Southwestern

cell line (*Homo sapiens*)	H2122	John Minna		UT Southwestern
cell line (*Homo sapiens*)	H2126	John Minna		UT Southwestern
cell line (*Homo sapiens*)	H1944	John Minna		UT Southwestern
cell line (*Homo sapiens*)	HCC515	John Minna		UT Southwestern
cell line (*Homo sapiens*)	HCC1195	John Minna		UT Southwestern
antibody	anti-COX6B2 (Rabbit polyclonal)	MilliporeSigma	Cat# SAB1401983, RRID:AB_10609550	IB (1:1000) IF (1:50) IHC (1:150)
antibody	anti-COX6B1 (Mouse monoclonal)	Santa Cruz Biotechnology	Cat# sc-393233, RRID:AB_2814984	IB (1:1000)
antibody	anti-COXIV (Rabbit monoclonal)	Cell Signaling Technology	Cat# 4850, RRID:AB_2085424	IB (1:5000) IF (1:200)
antibody	anti-β-Actin (Mouse monoclonal)	Santa Cruz Biotechnology	Cat# sc-47778	IB (1:10,000)
antibody	anti-V5 (Mouse monoclonal)	Thermo Fisher Scientific	R960-25; RRID:AB_2556564	IB (1:5000)
antibody	anti-HIF-1α (Mouse monoclonal)	BD Biosciences	Cat# 610959, RRID:AB_398272	IB (1:1000)
antibody	anti-Cleaved Caspase-3 (Rabbit polyclonal)	Cell Signaling Technology	Cat# 9661, RRID:AB_2341188	IB (1:500)

antibody	anti-PARP (Rabbit monoclonal)	Cell Signaling Technology	Cat# 9532, RRID:AB_659884	IB (1:1000)
antibody	anti-ERK (Mouse monoclonal)	Santa Cruz Biotechnology	Cat# sc-135900, RRID:AB_2141283	IB (1:3000)
antibody	anti-NDUFA9 (Mouse monoclonal)	Thermo Fisher Scientific	Cat# 459100, RRID:AB_2532223	IB (1:1000)
antibody	anti-UQCRC2 (Mouse monoclonal)	Abcam	Cat# ab14745, RRID:AB_2213640	IB (1:1000)
antibody	Anti-Tom20 (Mouse monoclonal)	Santa Cruz Biotechnology	Cat# sc-17764, RRID:AB_628381	IF (1:200)
commercial assay or kit	MitoTracker™ Green	Thermo Fisher Scientific	M7514	
commercial assay or kit	MitoSOX Red™	Thermo Fisher Scientific	M36008	
commercial assay or kit	MitoProbe™ JC-1	Thermo Fisher Scientific	M34152	
commercial assay or kit	Cell-Titer Glo®	Promega	PR-G7572	
commercial assay or kit	NAD^+/NADH-Glo Assay™	Promega	G9071	
commercial assay or kit	Click-iT™ EdU Alexa Fluor 488 Imaging Kit	Thermo Fisher Scientific	C10037	

commercial assay or kit	Senescence Beta-Galactosidase Staining Kit	Cell Signaling Technology	9860	
commercial assay or kit	Colloidal Blue Staining Kit	Thermo Fisher Scientific		
chemical compound, drug	oligomycin	MilliporeSigma	O4876	
chemical compound, drug	CCCP	MilliporeSigma	C2759	
chemical compound, drug	antimycin A	MilliporeSigma	A8674	
chemical compound, drug	Seahorse XF Plasma Membrane Permeabilize	Agilent	102504-100	
chemical compound, drug	NAC	MilliporeSigma	N7250	
chemical compound, drug	Saponin	MilliporeSigma	47036	
software, algorithm	FlowJo®	FlowJo®	RRID:SCR_008520	ver 10
software, algorithm	ImageJ (Fiji)	Schindelin et al. (2012)	RRID:SCR_002285	ver 2.0.0
software, algorithm	Integrative Genomics Viewer	Robinson et al. (2011)	RRID:SCR_011793	ver 2.3.93

364

365 **Cell lines**

366 All NSCLC cell lines were obtained from John Minna (UT Southwestern) between 2014
367 and 2018. NSCLC cells were cultured in RPMI media supplemented with 5% FBS at 37°C,
368 5% CO_2 and 90% humidity. NSCLC cells were not passaged more than 10 times after
369 thawing. Cells cultured under hypoxia followed the methods described previously (Wright
370 and Shay 2006), and each chamber attained oxygen concentration of ~2.5%. HEK293T
371 cells were obtained from ATCC in 2014 and cultured in DMEM media supplemented with
372 10% FBS at 37°C, 5% CO_2 and 90% humidity. HEK293T cells were not passaged more
373 than 3 times after thawing. All cells were authenticated between 2014 and 2020 using
374 short tandem repeat profiling and periodically evaluated for mycoplasma contamination
375 by DAPI stain for extra-nuclear DNA within one year of use.

376

377 **Reagents**

378 Chemicals and reagents were purchased from the following manufacturers: RPMI-1640
379 medium (R8758), DMEM (D6429), fetal bovine serum (FBS; F0926, batch# 17J121),
380 HBSS (H8264), EGTA (E3889), fatty acid free BSA (A7030), oligomycin (O4876), CCCP
381 (C2759), antimycin A (A8674), mannitol (M4125), KH_2PO_4 (P0662), $MgCl_2$ (M8266), ADP-
382 K^+ salt (A5285), ascorbate (A5960), *N,N,N′,N′*-Tetramethyl-*p*-phenylenediamine
383 dihydrochloride (TMPD; 87890), sodium pyruvate solution (S8636), L-glutamine (G7513),
384 dodecyltrimethylammonium bromide (DTBA; D8638), DAPI (D9542), saponin (47046),
385 (uridine (U3003), and *N*-Acetyl-L-cysteine (NAC, N7250) were purchased from
386 MilliporeSigma. HEPES (BP410), sucrose (50-712-768), EDTA (S311), Tris Base

387 (BP152), formaldehyde (BP521), and Hoechst 3342 (PI62249) were purchased from
388 Fisher Scientific. Seahorse XF Plasma Membrane Permeabilizer (XF PMP; 102504-100)
389 are from Agilent.
390
391 **Normal lung lysate and human LUAD tissues**
392 Human normal lung whole tissue lysate was purchased from Novus Biologicals (NB820-
393 59237). All human LUAD tissues were obtained from the UTSW Tissue Resource in
394 compliance with guidelines for informed consent approved by the UTSW Internal Review
395 Board committee. Samples were homogenized in RIPA buffer (50 mM Tris-HCl pH7.4,
396 150 mM NaCl, 1% Triton X-100, 0.5% Sodium Deoxycholate, 0.1% SDS, 1 mM EDTA,
397 10 mM NaF, 1μg ml^{-1} pepstatin, 2μg ml^{-1} leupeptin, 2μg ml^{-1} aprotinin and 50μg ml^{-1}
398 bestatin). The protein was recovered by centrifuge and quantitated by Pierce™ BCA
399 Protein Assay Kit (23227, Thermo Fisher Scientific).
400
401 **Kaplan-Meier analysis**
402 Overall survival and time to first progression graphs were generated using kmplotter
403 **(**http://www.kmplot.com/lung) (Gyorffy et al. 2013). In NSCLC, probability of overall
404 survival (OS) was based on 1144 patients and time to first progression (FP) in 596
405 patients. In lung andenocarcinoma (LUAD), OS was based on 672 patients and FP on
406 443 patients. In lung squamous carcinoma (LUSC), OS was based on 271 patients and
407 FP on 141 patients. Hazard ratios and p-values were calculated by Cox Regression
408 Analysis.
409

410 **TCGA data analysis**

411 We used the UCSC Xena program (https://xenabrowser.net) to download RNA-Seq data
412 from the cohort of TCGA Lung Cancer (LUNG). Values were analyzed using Prism
413 Graphpad software (v 8.4.3).

414

415 **Immunoblotting**

416 SDS-PAGE and immunoblotting were performed as previously described (Maxfield et al.
417 2015). Antibodies used for immunoblotting were as follows: COX6B2 (1:1000,
418 SAB1401983, MilliporeSigma), COX6B1 (1:1000, sc-393233, Santa Cruz Biotechnology),
419 COXIV (1:5000, 4850, Cell Signaling Technology), β-Actin (1:10,000, sc-47778, Santa
420 Cruz Biotechnology), V5 (1:5000, R960-25, Thermo Fisher Scientific), HIF-1α (1:1000,
421 610959, BD Biosciences), Cleaved Caspase-3 (1:500, 9661, Cell Signaling Technology),
422 PARP (1:1000, 9532, Cell Signaling Technology), ERK (1:3000, sc-135900, Santa Cruz
423 Biotechnology), NDUFA9 (1:1000, 459100, Thermo Fisher Scientific), UQCRC2 (1:1000,
424 ab14745, Abcam). Proteins were quantitated by ImageJ software and normalized to
425 CTRL groups. Incorporated COX6B1, COX6B2 or COXIV in individual complex
426 (monomers (IV) and dimers (IV_2) and supercomplexes (III_2+IV and I+III_2+IV_n)) was
427 normalized to total complexes (sum of IV, IV_2, III_2+IV and I+III_2+IV_n).

428

429 **Immunofluorescence**

430 Cells plated on glass coverslips were washed with PBS, fixed with 4% formaldehyde for
431 15 minutes at room temperature and blocked for 3 hours at room temperature in blocking
432 buffer (5% BSA in PBS with 0.1% Saponin). Cells were incubated with primary antibodies

433 diluted with blocking buffer overnight at 4°C followed by washes and incubation with Alexa
434 Fluor®-conjugated secondary antibodies (Thermo Fisher Scientific) for 1 hour at room
435 temperature. ProLong™ Gold Antifade reagent with DAPI (Thermo Fisher Scientific) was
436 used to mount slips on glass slides and images were acquired by Zeiss LSM510 confocal
437 microscope or Leica DM5500 B upright microscope. Antibodies used: COX6B2 (1:50,
438 SAB1401983, MilliporeSigma), Tom20 (1:200, sc-17764, Santa Cruz Biotechnology),
439 COXIV (1:200, 4850, Cell Signaling Technology). Staining was quantitated using ImageJ
440 software.
441
442 **Human lung tissue immunohistochemistry (IHC)**
443 Non-malignant testis, lung and LUAD tissues were obtained with informed consent from
444 the UTSW Tissue Management Shared Resource (TMSR) in compliance with the UTSW
445 Internal Review Board committee. COX6B2 IHC was optimized and performed by the
446 TMSR according to internal protocols using the Dako Autostainer Link 48 system. Briefly,
447 the slides were baked for 20 minutes at 60°C, then deparaffinized and hydrated before
448 the antigen retrieval step. Heat-induced antigen retrieval was performed at low pH for 20
449 minutes in a Dako PT Link. The tissue was incubated with a peroxidase block and then
450 an antibody incubated (COX6B2; 1:150, SAB1401983, MilliporeSigma) for 35
451 minutes. The staining was visualized using the EnVision FLEX visualization system.
452 Staining scores of COX6B2 ranging from 0 to 3 were set based on the positive scores
453 quantitated by using IHC Profiler of ImageJ (Varghese et al. 2014): score 0 (<30), score
454 1(30-45), score 2 (45-60), and score 3 (>60). Figure 1G demonstrates a 0 for negative
455 staining whereas score 3 shows the highest staining intensity.

456

457

458 **Expression plasmids**

459 Human COX6B2 and COX6B1 were obtained in pDONR223 (DNASU) and cloned into
460 pLX302 and pLX304 respectively using the Gateway® Cloning system (Thermo Fisher
461 Scientific). psPAX2 and pMD2.G lentiviral constructs were purchased from Addgene.
462 For shRNA experiments, pLKO.1 vectors from TRC expressing COX6B2-targeted
463 shRNAs (TRCN0000046119-122; sequences: 5'-CCGGGAGCAGATCAAGAACGGGAT
464 TCTCGAGAATCCCGTTCTTGATCTGCTCTTTTTG-3', 5'-CCGGGATCCGTAACTGCT
465 ACCAGAACTCGAGTTCTGGTAGCAGTTACGGATCTTTTTG-3', 5'-CCGGCTACCAGA
466 ACTTCCTGGACTACTCGAGTAGTCCAGGAAGTTCTGGTAGTTTTTG-3', 5'-CCGGCC
467 AGCCAGAACCAGATCCGTACTCGAGTACGGATCTGGTTCTGGCTGGTTTTTG-
468 3') were used as shRNA pool. Nontargeting shRNA in pLKO.1 (shSCR) was used as a
469 control (Addgene). For sgRNA experiments, pSpCas9(BB)-2A-GFP (PX458) was
470 purchased from Addgene.

471

472 **Lentiviral transduction**

473 Lentivirus was produced through co-transfection of HEK293T cells with 5 μg of viral
474 expression vector, 3 μg of psPAX2 packing vector, and 2 μg of pMD2.G envelope vector.
475 Virus-conditioned medium was harvested, passed through 0.45-μm-pore-size filters, and
476 then used to infect target cells in the presence of 10 μg/ml Sequa-brene™ (S2667,
477 MilliporeSigma).

478

479 **Mitochondrial content and mass analysis**

480 Mitochondrial DNA quantification was performed as described (de Almeida et al. 2017).
481 To detect mitochondrial mass, cells were incubated with 50 nM MitoTracker™ Green
482 (Fisher Scientific) at 37°C for 25 minutes and processed according to manufacturer's
483 protocol. A minimum of 20,000 cells were analyzed by flow cytometry using a BD
484 LSRFortessa™ instrument and BD FACSDiva™ 6.2 software. Data were analyzed by
485 FlowJo® (v10). The median fluorescent intensities in each group were used to calculate
486 the fold change compared to the CTRL group.

487

488 **Metabolic assays**

489 The oxygen consumption rate (OCR) and extracellular acidification rate (ECAR) were
490 performed by using the Seahorse Xfe96 Extracellular Flux analyzer (Agilent). Cells were
491 plated in the Xfe96 cell culture plates at a density of 10,000 cells (HCC515) or 5000 cells
492 (H2122) in 80 μl of growth medium overnight to generate a confluent monolayer of cells.
493 The assay medium consisted of 10mM glucose, 2mM glutamine, 1mM pyruvate in DMEM
494 (D5030, MilliporeSigma). The reaction was monitored upon serial injections of oligomycin
495 (5 μM), CCCP (1 μM), and antimycin A (2 μM). Results were normalized to total protein
496 amount as determined by Pierce™ BCA Protein Assay Kit. Non-mitochondrial respiration
497 is subtracted from the presented data. COX6B2 depleted cells were assessed following
498 eight days of shRNA or three days of siRNA. Complex IV activity of isolated mitochondria
499 was directly assessed in permeabilized cells as described (Salabei, Gibb, and Hill 2014;
500 Divakaruni, Rogers, and Murphy 2014), except that cells were permeabilized by XF PMP

501 (1nM). Complex III was inhibited with antimycin A (2μM) and then treated with complex
502 IV substrates (Ascorbate 10mM, TMPD 100μM) **(Figure 3A)**.
503
504 **Measurement of ATP**
505 Cell-Titer Glo® (Promega) (CTG) was performed by manufacture's protocol but modified
506 to use 15 μl of CTG for 100 μl of cells in media. Data were normalized to total protein
507 amount as determined by Pierce™ BCA Protein Assay Kit. Luminescence was read using
508 a Pherastar® Plus plate reader (BMG Labtech).
509
510 **NAD^+/NADH assay**
511 Cells were plated into 96-well tissue culture plates (Corning), allowed to adhere overnight
512 and reach 80-90% confluency. Cells were processed according to the manufacturer's
513 protocols for NAD^+/NADH-Glo Assay™ (Promega) with modification as previously
514 described (Gui et al. 2016). NAD^+/NADH measured in COX6B2 depleted cells were
515 transduced with shRNA for 8 days.
516
517 **Blue native PAGE (BN-PAGE)**
518 Mitochondria isolation and BN-PAGE were performed as previously described (Jha,
519 Wang, and Auwerx 2016; Wittig, Braun, and Schagger 2006; Ikeda et al. 2013). The
520 protocol was modified in that mitochondrial fractions were collected in buffer containing
521 200 mM sucrose, 10 mM Tris and 1mM EGTA/Tris. Mitochondria (50 μg) were solubilized
522 in 20 μl buffer containing 50 mM NaCl, 50 mM Imidazole/HCl, 2 mM 6-Aminocaproic acid,
523 1mM EDTA, and digitonin (digitonin/protein ratio of 6g/g) for 30 minutes at 4°C.

524 Solubilized proteins were supplemented with Coomassie brilliant blue G-250
525 digitonin/Coomassie dye in a ratio of 4:1, separated on NativePAGE™ Bis-Tris gels (3-
526 12%, Thermo Fisher Scientific), and stained by Colloidal Blue (Thermo Fisher Scientific)
527 or immunoblotted. NativeMark™ Unstained Protein Standard (Thermo Fisher Scientific)
528 was used as a marker (Mourier et al. 2014).
529
530 **Measurement of reactive oxygen species (ROS)**
531 The Fluorescent probe MitoSOX Red™(ThermoFisher) was used to measure superoxide.
532 MitoSOX Red™ is a mitochondrial membrane dependent dye and therefore could not be
533 used in COX6B2 depleted cells as they lose mitochondrial membrane potential ($\Delta\Psi_m$). In
534 this case, Chloromethyldichlorodihydrofluorescein diacetate (CM-H2DCFDA, Fisher
535 Scientific), detecting H_2O_2, was used for total ROS analysis in cells 11 days of shRNA
536 silencing. For MitoSOX Red™ assay, 3 x 10^5 cells were stained by MitoSOX Red™ (5
537 μM; in HBSS) at 37°C for ten minutes. As a positive control, cells were treated with 50
538 μM antimycin A during staining. For H_2O_2 measurements, cells reaching approximately
539 80% confluency in 6-well dishes were stained by CM-H2DCFDA (5 μM; in HBSS) at 37°C
540 for 20 minutes, washed with HBSS, and then recovered in culture media at 37°C for 15
541 minutes. Cells were immediately analyzed by flow cytometry using a BD LSRFortessa™
542 instrument and BD FACSDiva™ 6.2 software. A minimum of 20,000 cells were analyzed
543 per condition. Data were analyzed by FlowJo® (v10). Forward scatter (FSC) and side
544 scatter (SSC) parameters were used to exclude cellular debris, dead cells, and doublets
545 to retain viable single cell events. The median fluorescent intensities in each group were
546 used to calculate the fold change compared to the CTRL group. CM-H2DCFDA had to be

547 used in COX6B2 depleted cells because MitoSOX Red™ is dependent upon
548 mitochondrial integrity, which is lost under these conditions (Zielonka and Kalyanaraman
549 2010).
550
551 **EdU incorporation assays**
552 Cells were exposed to ethynyl deoxyuridine (EdU) for 1 hour before fixing the cells in 4%
553 formaldehyde. Cells were stained using the protocol for Click-iT™ EdU Alexa Fluor 488
554 Imaging Kit (Thermo Fisher) and co-stained with Hoechst 3342. Cells were quantified
555 using fluorescence microscopy. EdU detected in COX6B2 depleted cells were transduced
556 with shRNA for nine days.
557
558 **Proliferation measurements**
559 Cell proliferation was measured as described (Gui et al. 2016). HCC515 and H2122 cells
560 were plated in replicates in 96-well plate with an initial seeding density of 1,200 cells and
561 700 cells respectively. The proliferation rate was calculated using the following formula:
562 Proliferation Rate (Doublings per day) = Log_2 (Final cell count (day 5)/Initial cell count
563 (day 1))/4 (days).
564
565 **Soft-agar assays**
566 Cells were seeded at a density of 50,000 cells (HCC515) or 5000 cells (H2122) per 12-
567 well plate and treated as previously described (Gallegos et al. 2019). After three weeks,
568 colonies were stained overnight with 0.01% crystal violet. Images were captured with a
569 dissecting microscope, and quantitated by ImageJ software.

570

571 **Gene expression**

572 RNA was isolated using a mammalian total RNA isolation kit (RTN350, Sigma) and
573 treated with Dnase I (AMPD1, Sigma) according to the manufacturer's instructions. Equal
574 microgram volumes of RNA were reverse transcribed for each experimental condition by
575 the use of a High-Capacity cDNA reverse transfection kit (4368813, ThermoFisher
576 Scientific) with oligo dT (12577-011, ThermoFisher Scientific). The resulting cDNA was
577 used for expression analysis performed with an Applied Biosystems real-time PCR
578 system with TaqMan® real-time PCR probes (Thermo Fisher). The TaqMan® qPCR
579 probes were as follows: COX6B2 (Hs00376070_m1), COX6B1 (Hs01086739_g1).
580 RPL27 (Hs03044961_g1) was used as an internal loading assay for all expression assays.

581

582 **HIF-1 chromatin immunoprecipitation (ChIP) dataset analysis**

583 Raw reads were obtained from GSE59937 (Zhang et al. 2015) and aligned to the human
584 genome (hg19) using Bowtie2 with the 'sensitive' parameters enabled. SAMtools was
585 used to sort and index mapped read files, which were then converted to bigWig files
586 (DeepTools) for visualization on the IGV genome browser (Robinson et al. 2011).

587

588 **Transfections**

589 siRNAs were reverse transfected with Lipofectamine® RNAiMAX (13778, Thermo Fisher
590 Scientific) following the manufacturer's instructions. siRNAs against COX6B2 (sense
591 sequence: COX6B2#1: 5'-GGAACGAGCAGATCAAGAA-3'; COX6B2#2: 5'-
592 GCCAGAACCAGATCCGTA A-3') were purchased from Dharmacon and Sigma

593 respectively. siGENOME Non-Targeting siRNA Pool #2 was used as a negative control
594 (siCTRL). sgRNAs were forward transfected in 6-well dishes by using 6 μl of FuGENE®
595 HD (PRE2311, Fisher Scientific) with 3 μg of sgRNA. Guide sequences of COX6B2
596 sgRNA are as following:
597 oligo #1: 5'-CACCGCGGCGTCGAC CATTTCCCCTTGG-3',
598 oligo #2: 5'-CACCGCGTCGACCATTTCCCCTTGGGG-3',
599 oligo #3: 5'-CACCGACATCCAACATCCACGAAGGAGG-3'.
600

601 **Measurement of mitochondrial membrane potential**

602 Following six days of shRNA (3 x 10^5 cells), cells were collected and resuspended in
603 HBSS containing 0.2 μM JC-1 and incubated at 37°C in a CO_2 incubator for 25 minutes.
604 The stained cells were collected by centrifuge and washed twice with HBSS containing
605 1% FBS. Then cells were resuspended in 500 μl of 1% FBS HBSS buffer. Cells were
606 immediately analyzed by flow cytometry using a BD LSRFortessa™ instrument and BD
607 FACSDiva™ 6.2 software. A minimum of 20,000 cells were analyzed per condition.
608 FlowJo® (v10) was used to generate scatter plots.
609

610 **Annexin-V staining**

611 After 7 days of shRNA-mediated knockdown 1 x 10^5 cells were wash once in PBS and
612 resuspend in Annexin-V Binding Buffer (422201, BioLegend) with 3 μl of Annexin-V-APC
613 (640941, BioLegend) and DAPI (200 ng/ml), and incubated for 15 minutes at room
614 temperature in the dark. Cells were immediately analyzed by flow cytometry using a BD
615 LSRFortessa™ instrument and BD FACSDiva™ 6.2 software. A minimum of 20,000 cells

616 were analyzed per condition. FlowJo® (v10) was used to generate scatter plots. Early-
617 stage apoptotic cells are presented in the lower right quadrants (Annexin-V positive and
618 DAPI negative) and late-stage apoptotic cells are presented in the upper right quadrants
619 (Annexin-V positive and DAPI positive).
620

621 **Senescence associated β-galactosidase activity**

622 Cells were stained by using Senescence Beta-Galactosidase Staining Kit following 11
623 days of shRNA (9860, Cell Signaling Technology) according to the manufacture's protocol.
624 Cultures were examined under phase-contrast microscopy to determine the percentage
625 of positive cells with blue precipitate.
626

627 **Xenograft experiments**

628 All animal experiments were conducted under a UT-Southwestern IACUC approved
629 protocol. Hsd:Athymic Nude-Foxn1^{nu} female mice were purchased from Envigo. At six to
630 eight-weeks of age (23-25 grams) mice were randomly assigned to the indicated groups.
631 Sample size was determined by the formula: $n = 1+2C(s/d)^2$, in which C = 10.51, based
632 on a power of 90% and a confidence interval of 95%, S = standard deviation of tumor
633 volume (20%), D=tumor burden difference to be considered significant (50%). Therefore,
634 five mice per condition were tested. 2×10^6 cells in 100 µl PBS were subcutaneously
635 injected in the flank. Once tumors were visible, tumor volume was measured by caliper in
636 two dimensions, and volumes were estimated using the equation $V = \text{length} \times \text{width}^2/2$.
637 Caliper measurements were made twice a week.
638

639 **Statistical analysis**

640 Graphpad Prism (Graphpad Software) was used to perform all statistical analyses. Data
641 were assessed for normality by Shapiro-Wilk tests. Unpaired Student's *t*-test was used
642 for data with a normal distribution. Mann-Whitney test was used for data that did not
643 conform to a normal distribution. *P* values less than or equal to 0.050 were considered
644 significant. Biological replicates represent experiments performed on samples from
645 separate biological preparations; technical replicates represent samples from the same
646 biological preparation run in parallel.

647

648 **ACKNOWLEDGEMENTS**

649 The authors thank Melanie Cobb for critical review of the manuscript and Jonathan
650 Friedman for technical suggestions. AWW, CC, ZG and KM were supported by NIH
651 (R01CA196905). AWW and JW were supported by SU2C (SU2C-AACR-IRG1211).
652 Samples were obtained and stained with the help of the UTSW tissue
653 management shared resource, which is supported by the Simmons Cancer
654 Center Core grant from National Cancer Institute (P30CA142543).

655

656

657 FIGURE LEGENDS

658 **Figure 1. COX6B2 mRNA expression correlates with poor outcome in LUAD. (A-C)**
659 Kaplan-Meier curves for OS and FP in NSCLC (A) LUAD (B) and LUSC patients (C). **(D)**
660 COX6B2 mRNA expression (RNA-seq RSEM, log2(norm count +1)) from TCGA Lung
661 Cancer dataset. Bars represent median (normal: n = 110; tumor: n = 1017). *P* values

662 calculated by Mann-Whitney test. **(E-F)** Whole tissue homogenates of LUAD tumors (E)
663 and LUAD cell line lysates (F) were immunoblotted with indicated antibodies. Molecular
664 weight (MW) markers are indicated. **(G)** IHC staining of non-malignant testis (a positive
665 control), non-malignant lung (adjacent normal) and LUAD tissues. Scores ranged from 0
666 to 3. Scale bar, 50 μm. Bars represent mean ± SEM. *P* values calculated by Mann-
667 Whitney test. **(H)** Representative confocal images of endogenous COX6B2 in HCC515
668 cells. Tom20 is used as a mitochondrial marker. Images were shown as Z-stack maximum
669 projection from 0.3 μm-thick-image. Scale bar, 10 μm.
670
671 **Figure 2. COX6B2 expression enhances mitochondrial respiratory activity. (A)** Left:
672 Whole cell lysates from HCC515 cells +/- COX6B2-V5 were immunoblotted with indicated
673 antibodies. MW markers are indicated. Right: Quantitation of COX6B2 protein expression
674 from blots on left. Bars represent mean ± SD (n = 4). **(B)** Mitochondrial DNA content. Bars
675 represent mean + range (n = 2). **(C)** Quantification of total mitochondria using FACS
676 analysis of Mitotracker green stained cells. Bars represent mean ± SD (n = 3). **(D)** Left:
677 Oxygen consumption rate (OCR) as a function of time in indicated cell lines following
678 exposure to electron transport chain complex inhibitors. Bars represent mean ± SEM (n
679 = 6). Right: Mean and distribution of individual values for basal, ATP-linked, maximal and
680 reserve OCRs. *P* values calculated by Student's *t*-test. **(E)** Left: Whole cell lysates from
681 H2122 cells +/- COX6B2-V5 were immunoblotted with indicated antibodies. MW markers
682 are indicated. Right: Quantitation of COX6B2 protein expression. Bars represent mean ±
683 SD (n = 3). **(F)** As in (D) (n = 8). **(G)** ATP content of indicated cell lines. Bars represent
684 mean + SEM (n ≥ 6). HCC515 *P* value calculated by Student's *t*-test and H2122 *P* value

685 calculated by Mann-Whitney test. **(H)** NAD^+/NADH measurement in indicated cell lines.
686 Bars represent mean ± SEM (n ≥ 5). *P* value calculated by Student's *t*-test. **(I)** Basal
687 extracellular acidification rate (ECAR) are presented as mean ± SEM (n ≥ 6) from CTRL
688 and COX6B2-V5 cells of HCC515 and H2122 cells. *P* value calculated by Student's *t*-test.
689 **(J)** Immunoblots of indicated whole cell lysates with specified antibodies. MW markers
690 are indicated. **(K)** As in (D) using indicated cell lines. Bars represent mean ± SEM (n ≥
691 9). Basal and ATP-link OCR *P* value calculated by Student's *t*-test. Maximal OCR and
692 reserve capacity *P* value calculated by Mann-Whitney test.
693
694 **Figure 3. COX6B2 enhances complex IV activity of OXPHOS without increasing**
695 **ROS production. (A)** Schematic of complex IV activity measurements in isolated
696 mitochondria. Details are described in Material and Methods. antA, Antimycin A; Cyt c,
697 Cytochrome c; ATP Syn, ATP synthase. **(B)** Complex IV activity in indicated cell lines
698 using TMPD/ascorbate as a substrate. Bars represent mean + SEM (n ≥ 8). *P* value
699 calculated by Student's *t*-test. **(C)** As in (B) in HCC515 cell lines expressing CTRL and
700 COX6B1-V5 cDNA. Bars represent mean + SEM (n = 8). *P* value calculated by Student's
701 *t*-test. **(D)** Indicated lysates from HCC515 cells were run on a BN-PAGE gel and stained
702 with Colloidal Blue (left two panels) or immunoblotted with anti-COX6B2, anti-COX6B1
703 and anti-COXIV (right panels). Representative image of n ≥ 3. MW markers are indicated
704 to identify different complexes (Mourier et al. 2014). **(E)** Left: Distribution of COX6B1 and
705 COX6B2 incorporated in complex IV monomers, dimers or supercomplexes as detected
706 by BN-PAGE in (D). Right: Bars represent mean ± SEM (n ≥ 3) based on quantification
707 of bands in (D). In monomeric complex IV, *P* value calculated by Mann-Whitney test

708 whereas others calculated by Student's *t*-test. **(F)** Left: Distribution of COX6B1/COX6B2
709 incorporated in monomeric complex IV, dimeric complex IV and supercomplexes based
710 on BN-PAGE in COX6B2-V5 or COX6B1-V5 overexpressing cell lines (D). Right: Bars
711 represent mean ± SEM (n ≥ 3) based on quantification of bands in (D). In monomeric
712 complex IV, *P* value calculated by Mann-Whitney test whereas others calculated by
713 Student's *t*-test. **(G)** Left: Distribution of COXIV incorporated in monomeric complex IV,
714 dimeric complex IV and supercomplexes by blots from (D)**.** Right: Bars represent mean ±
715 SEM (n ≥ 3) of COXIV based on quantification of band in (D). *P* value calculated by
716 Student's *t*-test. **(H)** Relative superoxide in indicated cell lines. Bars represent mean +
717 SEM (n = 5). *P* value calculated by Student's *t*-test.
718
719 **Figure 4. COX6B2 promotes cell division. (A)** Percentage of cells positive for EdU
720 incorporation in indicated samples. Values represent the mean ± SEM (n ≥ 9). *P* value
721 calculated by Student's *t*-test. **(B)** Population doubling rate in indicated samples incubated
722 ± 1mM pyruvate for five days. Bars represent mean + SEM (n = 4). *P* value calculated
723 by Student's *t*-test. **(C)** Top: Representative images of soft agar assays for indicated cell
724 lines. Arrows indicate formed colonies. Bottom: Graphs represent mean colony numbers
725 in indicated cell lines. Bars represent mean ± SEM (n = 6). *P* value calculated by Student's
726 *t*-test. **(D)** EdU positive HCC515 cells at indicated times in hypoxia. Values are relative to
727 cells incubated in normoxia. Bars represent mean ± SEM (n = 8). *P* value calculated by
728 Student's *t*-test. **(E)** Average mRNA expression of COX6B2 measured following 12 hours
729 of hypoxia culture in HCC515 cells. Bars represent mean ± SEM (n = 6). *P* calculated by
730 Student's *t*-test. **(F)** Whole cell lysates from indicated cell lines were immunoblotted with

731 indicated antibodies. Hypoxia exposure was for 12 hours. Representative immunoblots
732 from n = 3. MW markers are indicated.
733
734 **Figure 5. Depletion of COX6B2 impairs mitochondrial function. (A-B)** Left: Oxygen
735 consumption rate (OCR) as a function of time in COX6B2 depleted HCC515 cells using
736 an shRNA pool (A) or an siRNA pool (B) following exposure to electron transport chain
737 complex inhibitors. Bars represent mean ± SEM (n ≥ 4). Right: Bars represent mean ±
738 SEM 20 minutes following the addition of each drug (on left). *P* values calculated by
739 Student's *t*-test. **(C)** Relative NAD^+/NADH measurement in indicated cell lines. Bars
740 represent mean + SEM (n = 4). *P* value calculated by Student's *t*-test. **(D)** Relative ATP
741 content in indicated cell lines transfected with indicated individual siRNAs for 96 hours.
742 Bars represent mean + SEM (n = 6), **** $P < 0.0001$; *** $P < 0.005$ calculated by Student's
743 *t*-test. **(E)** Left panels: Flow cytometry measurement following JC-1 labelling of indicated
744 HCC515 cells. Right graph: Bars represent mean of the aggregate to monomer ratio
745 (red/green) in indicated cell lines + SEM (n = 3). *P* value calculated by Student's *t*-test.
746 **(F)** Indicated cell lines were labelled with CM-H2DCFDA to measure H_2O_2 as described
747 in material and methods. Bars represent mean fold change in median fluorescent
748 intensities ± SEM (n = 4). *P* value calculated by Student's *t*-test.
749
750 **Figure 6. COX6B2 is essential for tumor cell viability and survival. (A)** Left:
751 Representative images of EdU staining in indicated cell lines. (EdU, green; Hoechst, blue).
752 Scale bar, 100 μm. Right: Quantitation of EdU-positive cells. Bars represent the mean ±
753 SEM (n ≥ 12). *P* value calculated by Student's *t*-test. (**B)** Left: Representative images of

754 colonies in soft agar. Arrows indicate formed colonies. Right: Bars represent relative
755 mean colony numbers ± SEM (n = 6). *P* value calculated by Student's *t*-test. **(C)**
756 Representative immunoblots of whole cell lysates of indicated cells blotted with indicated
757 antibodies. MW markers are indicated. **(D)** Left: Representative scatter plots of Annexin
758 V staining in indicated cell lines. Bars represent mean fold change + SEM (n = 6). *P*
759 calculated by Student's *t*-test. **(E)** Representative phase contrast images of indicated cell
760 lines. Arrowheads indicate the flattened senescence morphology with vacuole
761 accumulation and multinucleation. Scale bar, 100 μm. **(F)** Representative images of
762 senescence-associated- β-galactosidase staining in indicated cells. Scale bar, 100 μm.
763 Bars represent mean ± SEM (n ≥ 8). *P* calculated by Student's *t*-test. **(G)** Whole cell
764 lysates from indicated cell lines were cultured with or without NAC (5mM) for seven days
765 were immunoblotted with indicated antibodies. MW markers are indicated. **(H)**
766 Representative images of senescence-associated- β-galactosidase staining in indicated
767 cell lines cultured with or without NAC (5mM) for all 11 days. Scale bar, 100 μm. Bars
768 represent mean ± SEM (n = 9). *P* calculated by Student's *t*-test.
769
770 **Figure 7. COX6B2 supports tumor growth *in vivo*. (A and C)** Xenograft experiments
771 in indicated cell lines. Tumor volumes were measured using calipers on indicated days.
772 Each data point represents mean ± SEM (n = 5). *P* value calculated by Student's *t*-test.
773 **(B and D)** Left: Images of individual tumors (ruler indicates cm). Right: Mass of excised
774 tumors from indicated cell lines. Bars represent mean ± SEM (n = 5). *P* value calculated
775 by Student's *t*-test.
776

REFERENCES

Abdulhag, U. N., D. Soiferman, O. Schueler-Furman, C. Miller, A. Shaag, O. Elpeleg, S. Edvardson, and A. Saada. 2015. 'Mitochondrial complex IV deficiency, caused by mutated COX6B1, is associated with encephalomyopathy, hydrocephalus and cardiomyopathy', *Eur J Hum Genet*, 23: 159-64.

Acin-Perez, R., P. Fernandez-Silva, M. L. Peleato, A. Perez-Martos, and J. A. Enriquez. 2008. 'Respiratory active mitochondrial supercomplexes', *Mol Cell*, 32: 529-39.

Agarwal, A., G. Virk, C. Ong, and S. S. du Plessis. 2014. 'Effect of oxidative stress on male reproduction', *World J Mens Health*, 32: 1-17.

Balsa, E., M. S. Soustek, A. Thomas, S. Cogliati, C. Garcia-Poyatos, E. Martin-Garcia, M. Jedrychowski, S. P. Gygi, J. A. Enriquez, and P. Puigserver. 2019. 'ER and Nutrient Stress Promote Assembly of Respiratory Chain Supercomplexes through the PERK-eIF2alpha Axis', *Mol Cell*, 74: 877-90 e6.

Birsoy, K., T. Wang, W. W. Chen, E. Freinkman, M. Abu-Remaileh, and D. M. Sabatini. 2015. 'An Essential Role of the Mitochondrial Electron Transport Chain in Cell Proliferation Is to Enable Aspartate Synthesis', *Cell*, 162: 540-51.

de Almeida, M. J., L. L. Luchsinger, D. J. Corrigan, L. J. Williams, and H. W. Snoeck. 2017. 'Dye-Independent Methods Reveal Elevated Mitochondrial Mass in Hematopoietic Stem Cells', *Cell Stem Cell*, 21: 725-29 e4.

Divakaruni, A. S., G. W. Rogers, and A. N. Murphy. 2014. 'Measuring Mitochondrial Function in Permeabilized Cells Using the Seahorse XF Analyzer or a Clark-Type Oxygen Electrode', *Curr Protoc Toxicol*, 60: 25 2 1-16.

Fukuda, R., H. Zhang, J. W. Kim, L. Shimoda, C. V. Dang, and G. L. Semenza. 2007. 'HIF-1 regulates cytochrome oxidase subunits to optimize efficiency of respiration in hypoxic cells', *Cell*, 129: 111-22.

Gallegos, Z. R., P. Taus, Z. A. Gibbs, K. McGlynn, N. C. Gomez, I. Davis, and A. W. Whitehurst. 2019. 'EWSR1-FLI1 Activation of the Cancer/Testis Antigen FATE1 Promotes Ewing Sarcoma Survival', *Mol Cell Biol*, 39.

Gibbs, Z. A., and A. W. Whitehurst. 2018. 'Emerging Contributions of Cancer/Testis Antigens to Neoplastic Behaviors', *Trends Cancer*, 4: 701-12.

Gjerstorff, M. F., M. H. Andersen, and H. J. Ditzel. 2015. 'Oncogenic cancer/testis antigens: prime candidates for immunotherapy', *Oncotarget*, 6: 15772-87.

Gui, D. Y., L. B. Sullivan, A. Luengo, A. M. Hosios, L. N. Bush, N. Gitego, S. M. Davidson, E. Freinkman, C. J. Thomas, and M. G. Vander Heiden. 2016. 'Environment Dictates Dependence on Mitochondrial Complex I for NAD+ and Aspartate Production and Determines Cancer Cell Sensitivity to Metformin', *Cell Metab*, 24: 716-27.

Guieze, R., V. M. Liu, D. Rosebrock, A. A. Jourdain, M. Hernandez-Sanchez, A. Martinez Zurita, J. Sun, E. Ten Hacken, K. Baranowski, P. A. Thompson, J. M. Heo, Z. Cartun, O. Aygun, J. B. Iorgulescu, W. Zhang, G. Notarangelo, D. Livitz, S. Li, M. S. Davids, A. Biran, S. M. Fernandes, J. R. Brown, A. Lako, Z. B. Ciantra, M. A. Lawlor, D. B. Keskin, N. D. Udeshi, W. G. Wierda, K. J. Livak, A. G. Letai, D. Neuberg, J. W. Harper, S. A. Carr, F. Piccioni, C. J. Ott, I. Leshchiner, C. M. Johannessen, J. Doench, V. K. Mootha, G. Getz, and C. J. Wu. 2019. 'Mitochondrial Reprogramming Underlies Resistance to BCL-2 Inhibition in Lymphoid Malignancies', *Cancer Cell*, 36: 369-84 e13.

Gyorffy, B., P. Surowiak, J. Budczies, and A. Lanczky. 2013. 'Online survival analysis software to assess the prognostic value of biomarkers using transcriptomic data in non-small-cell lung cancer', *PLoS One*, 8: e82241.

Hayashi, T., Y. Asano, Y. Shintani, H. Aoyama, H. Kioka, O. Tsukamoto, M. Hikita, K. Shinzawa-Itoh, K. Takafuji, S. Higo, H. Kato, S. Yamazaki, K. Matsuoka, A. Nakano, H. Asanuma, M. Asakura, T. Minamino, Y. Goto, T. Ogura, M. Kitakaze, I. Komuro, Y.

827 Sakata, T. Tsukihara, S. Yoshikawa, and S. Takashima. 2015. 'Higd1a is a positive
828 regulator of cytochrome c oxidase', *Proc Natl Acad Sci U S A*, 112: 1553-8.
829 Helmlinger, G., F. Yuan, M. Dellian, and R. K. Jain. 1997. 'Interstitial pH and pO2 gradients in
830 solid tumors in vivo: high-resolution measurements reveal a lack of correlation', *Nat Med*,
831 3: 177-82.
832 Hunder, N. N., H. Wallen, J. Cao, D. W. Hendricks, J. Z. Reilly, R. Rodmyre, A. Jungbluth, S.
833 Gnjatic, J. A. Thompson, and C. Yee. 2008. 'Treatment of metastatic melanoma with
834 autologous CD4+ T cells against NY-ESO-1', *N Engl J Med*, 358: 2698-703.
835 Huttemann, M., S. Jaradat, and L. I. Grossman. 2003. 'Cytochrome c oxidase of mammals
836 contains a testes-specific isoform of subunit VIb--the counterpart to testes-specific
837 cytochrome c?', *Mol Reprod Dev*, 66: 8-16.
838 Ikeda, K., K. Horie-Inoue, T. Suzuki, R. Hobo, N. Nakasato, S. Takeda, and S. Inoue. 2019.
839 'Mitochondrial supercomplex assembly promotes breast and endometrial tumorigenesis
840 by metabolic alterations and enhanced hypoxia tolerance', *Nat Commun*, 10: 4108.
841 Ikeda, K., S. Shiba, K. Horie-Inoue, K. Shimokata, and S. Inoue. 2013. 'A stabilizing factor for
842 mitochondrial respiratory supercomplex assembly regulates energy metabolism in
843 muscle', *Nat Commun*, 4: 2147.
844 Jha, P., X. Wang, and J. Auwerx. 2016. 'Analysis of Mitochondrial Respiratory Chain
845 Supercomplexes Using Blue Native Polyacrylamide Gel Electrophoresis (BN-PAGE)',
846 *Curr Protoc Mouse Biol*, 6: 1-14.
847 Kadenbach, B., and M. Huttemann. 2015. 'The subunit composition and function of mammalian
848 cytochrome c oxidase', *Mitochondrion*, 24: 64-76.
849 Krisfalusi, M., K. Miki, P. L. Magyar, and D. A. O'Brien. 2006. 'Multiple glycolytic enzymes are
850 tightly bound to the fibrous sheath of mouse spermatozoa', *Biol Reprod*, 75: 270-8.
851 Li, S. S., D. A. O'Brien, E. W. Hou, J. Versola, D. L. Rockett, and E. M. Eddy. 1989. 'Differential
852 activity and synthesis of lactate dehydrogenase isozymes A (muscle), B (heart), and C
853 (testis) in mouse spermatogenic cells', *Biol Reprod*, 40: 173-80.
854 Lissanu Deribe, Y., Y. Sun, C. Terranova, F. Khan, J. Martinez-Ledesma, J. Gay, G. Gao, R. A.
855 Mullinax, T. Khor, N. Feng, Y. H. Lin, C. C. Wu, C. Reyes, Q. Peng, F. Robinson, A.
856 Inoue, V. Kochat, C. G. Liu, J. M. Asara, C. Moran, F. Muller, J. Wang, B. Fang, V.
857 Papadimitrakopoulou, Wistuba, II, K. Rai, J. Marszalek, and P. A. Futreal. 2018.
858 'Mutations in the SWI/SNF complex induce a targetable dependence on oxidative
859 phosphorylation in lung cancer', *Nat Med*, 24: 1047-57.
860 Maranzana, E., G. Barbero, A. I. Falasca, G. Lenaz, and M. L. Genova. 2013. 'Mitochondrial
861 respiratory supercomplex association limits production of reactive oxygen species from
862 complex I', *Antioxid Redox Signal*, 19: 1469-80.
863 Maxfield, K. E., P. J. Taus, K. Corcoran, J. Wooten, J. Macion, Y. Zhou, M. Borromeo, R. K.
864 Kollipara, J. Yan, Y. Xie, X. J. Xie, and A. W. Whitehurst. 2015. 'Comprehensive
865 functional characterization of cancer-testis antigens defines obligate participation in
866 multiple hallmarks of cancer', *Nat Commun*, 6: 8840.
867 Minton, D. R., L. Fu, N. P. Mongan, M. M. Shevchuk, D. M. Nanus, and L. J. Gudas. 2016. 'Role
868 of NADH Dehydrogenase (Ubiquinone) 1 Alpha Subcomplex 4-Like 2 in Clear Cell Renal
869 Cell Carcinoma', *Clin Cancer Res*, 22: 2791-801.
870 Mourier, A., S. Matic, B. Ruzzenente, N. G. Larsson, and D. Milenkovic. 2014. 'The respiratory
871 chain supercomplex organization is independent of COX7a2l isoforms', *Cell Metab*, 20:
872 1069-75.
873 Nayak, A. P., A. Kapur, L. Barroilhet, and M. S. Patankar. 2018. 'Oxidative Phosphorylation: A
874 Target for Novel Therapeutic Strategies Against Ovarian Cancer', *Cancers (Basel)*, 10.
875 Nichols, B. A., N. W. Oswald, E. A. McMillan, K. McGlynn, J. Yan, M. S. Kim, J. Saha, P. L.
876 Mallipeddi, S. A. LaDuke, P. A. Villalobos, J. Rodriguez-Canales, Wistuba, II, B. A.
877 Posner, A. J. Davis, J. D. Minna, J. B. MacMillan, and A. W. Whitehurst. 2018.

878 'HORMAD1 Is a Negative Prognostic Indicator in Lung Adenocarcinoma and Specifies
879 Resistance to Oxidative and Genotoxic Stress', *Cancer Res*, 78: 6196-208.
880 Odet, F., C. Duan, W. D. Willis, E. H. Goulding, A. Kung, E. M. Eddy, and E. Goldberg. 2008.
881 'Expression of the gene for mouse lactate dehydrogenase C (Ldhc) is required for male
882 fertility', *Biol Reprod*, 79: 26-34.
883 Oliva, C. R., T. Markert, G. Y. Gillespie, and C. E. Griguer. 2015. 'Nuclear-encoded cytochrome
884 c oxidase subunit 4 regulates BMI1 expression and determines proliferative capacity of
885 high-grade gliomas', *Oncotarget*, 6: 4330-44.
886 Rao, S., L. Mondragon, B. Pranjic, T. Hanada, G. Stoll, T. Kocher, P. Zhang, A. Jais, A. Lercher,
887 A. Bergthaler, D. Schramek, K. Haigh, V. Sica, M. Leduc, N. Modjtahedi, T. P. Pai, M.
888 Onji, I. Uribesalgo, R. Hanada, I. Kozieradzki, R. Koglgruber, S. J. Cronin, Z. She, F.
889 Quehenberger, H. Popper, L. Kenner, J. J. Haigh, O. Kepp, M. Rak, K. Cai, G. Kroemer,
890 and J. M. Penninger. 2019. 'AIF-regulated oxidative phosphorylation supports lung
891 cancer development', *Cell Res*, 29: 579-91.
892 Robinson, J. T., H. Thorvaldsdottir, W. Winckler, M. Guttman, E. S. Lander, G. Getz, and J. P.
893 Mesirov. 2011. 'Integrative genomics viewer', *Nat Biotechnol*, 29: 24-6.
894 Salabei, J. K., A. A. Gibb, and B. G. Hill. 2014. 'Comprehensive measurement of respiratory
895 activity in permeabilized cells using extracellular flux analysis', *Nat Protoc*, 9: 421-38.
896 Sampson, V., and T. Alleyne. 2001. 'Cytochrome c/cytochrome c oxidase interaction. Direct
897 structural evidence for conformational changes during enzyme turnover', *Eur J Biochem*,
898 268: 6534-44.
899 Schindelin, J., I. Arganda-Carreras, E. Frise, V. Kaynig, M. Longair, T. Pietzsch, S. Preibisch, C.
900 Rueden, S. Saalfeld, B. Schmid, J. Y. Tinevez, D. J. White, V. Hartenstein, K. Eliceiri, P.
901 Tomancak, and A. Cardona. 2012. 'Fiji: an open-source platform for biological-image
902 analysis', *Nat Methods*, 9: 676-82.
903 Scotland, S., E. Saland, N. Skuli, F. de Toni, H. Boutzen, E. Micklow, I. Senegas, R. Peyraud, L.
904 Peyriga, F. Theodoro, E. Dumon, Y. Martineau, G. Danet-Desnoyers, F. Bono, C.
905 Rocher, T. Levade, S. Manenti, C. Junot, J. C. Portais, N. Alet, C. Recher, M. A. Selak,
906 M. Carroll, and J. E. Sarry. 2013. 'Mitochondrial energetic and AKT status mediate
907 metabolic effects and apoptosis of metformin in human leukemic cells', *Leukemia*, 27:
908 2129-38.
909 Sinkler, C. A., H. Kalpage, J. Shay, I. Lee, M. H. Malek, L. I. Grossman, and M. Huttemann.
910 2017. 'Tissue- and Condition-Specific Isoforms of Mammalian Cytochrome c Oxidase
911 Subunits: From Function to Human Disease', *Oxid Med Cell Longev*, 2017: 1534056.
912 Smaili, S. S., Y. T. Hsu, K. M. Sanders, J. T. Russell, and R. J. Youle. 2001. 'Bax translocation
913 to mitochondria subsequent to a rapid loss of mitochondrial membrane potential', *Cell*
914 *Death Differ*, 8: 909-20.
915 Sullivan, L. B., D. Y. Gui, A. M. Hosios, L. N. Bush, E. Freinkman, and M. G. Vander Heiden.
916 2015. 'Supporting Aspartate Biosynthesis Is an Essential Function of Respiration in
917 Proliferating Cells', *Cell*, 162: 552-63.
918 Tai, H., Z. Wang, H. Gong, X. Han, J. Zhou, X. Wang, X. Wei, Y. Ding, N. Huang, J. Qin, J.
919 Zhang, S. Wang, F. Gao, Z. M. Chrzanowska-Lightowlers, R. Xiang, and H. Xiao. 2017.
920 'Autophagy impairment with lysosomal and mitochondrial dysfunction is an important
921 characteristic of oxidative stress-induced senescence', *Autophagy*, 13: 99-113.
922 Tsukihara, T., H. Aoyama, E. Yamashita, T. Tomizaki, H. Yamaguchi, K. Shinzawa-Itoh, R.
923 Nakashima, R. Yaono, and S. Yoshikawa. 1996. 'The whole structure of the 13-subunit
924 oxidized cytochrome c oxidase at 2.8 A', *Science*, 272: 1136-44.
925 Varghese, F., A. B. Bukhari, R. Malhotra, and A. De. 2014. 'IHC Profiler: an open source plugin
926 for the quantitative evaluation and automated scoring of immunohistochemistry images
927 of human tissue samples', *PLoS One*, 9: e96801.

928 Viphakone, N., M. G. Cumberbatch, M. J. Livingstone, P. R. Heath, M. J. Dickman, J. W. Catto,
929 and S. A. Wilson. 2015. 'Luzp4 defines a new mRNA export pathway in cancer cells',
930 *Nucleic Acids Res*, 43: 2353-66.
931 Weinberg, S. E., and N. S. Chandel. 2015. 'Targeting mitochondria metabolism for cancer
932 therapy', *Nat Chem Biol*, 11: 9-15.
933 Weishaupt, A., and B. Kadenbach. 1992. 'Selective removal of subunit VIb increases the activity
934 of cytochrome c oxidase', *Biochemistry*, 31: 11477-81.
935 Wittig, I., H. P. Braun, and H. Schagger. 2006. 'Blue native PAGE', *Nat Protoc*, 1: 418-28.
936 Wright, W. E., and J. W. Shay. 2006. 'Inexpensive low-oxygen incubators', *Nat Protoc*, 1: 2088-
937 90.
938 Zhang, J., C. Wang, X. Chen, M. Takada, C. Fan, X. Zheng, H. Wen, Y. Liu, C. Wang, R. G.
939 Pestell, K. M. Aird, W. G. Kaelin, Jr., X. S. Liu, and Q. Zhang. 2015. 'EglN2 associates
940 with the NRF1-PGC1alpha complex and controls mitochondrial function in breast
941 cancer', *EMBO J*, 34: 2953-70.
942 Zhang, K., G. Wang, X. Zhang, P. P. Huttemann, Y. Qiu, J. Liu, A. Mitchell, I. Lee, C. Zhang, J.
943 S. Lee, P. Pecina, G. Wu, Z. Q. Yang, M. Huttemann, and L. I. Grossman. 2016.
944 'COX7AR is a Stress-inducible Mitochondrial COX Subunit that Promotes Breast Cancer
945 Malignancy', *Sci Rep*, 6: 31742.
946 Zielonka, J., and B. Kalyanaraman. 2010. 'Hydroethidine- and MitoSOX-derived red
947 fluorescence is not a reliable indicator of intracellular superoxide formation: another
948 inconvenient truth', *Free Radic Biol Med*, 48: 983-1001.
949 Zu, X. L., and M. Guppy. 2004. 'Cancer metabolism: facts, fantasy, and fiction', *Biochem*
950 *Biophys Res Commun*, 313: 459-65.
951

Cheng et al. Figure 1

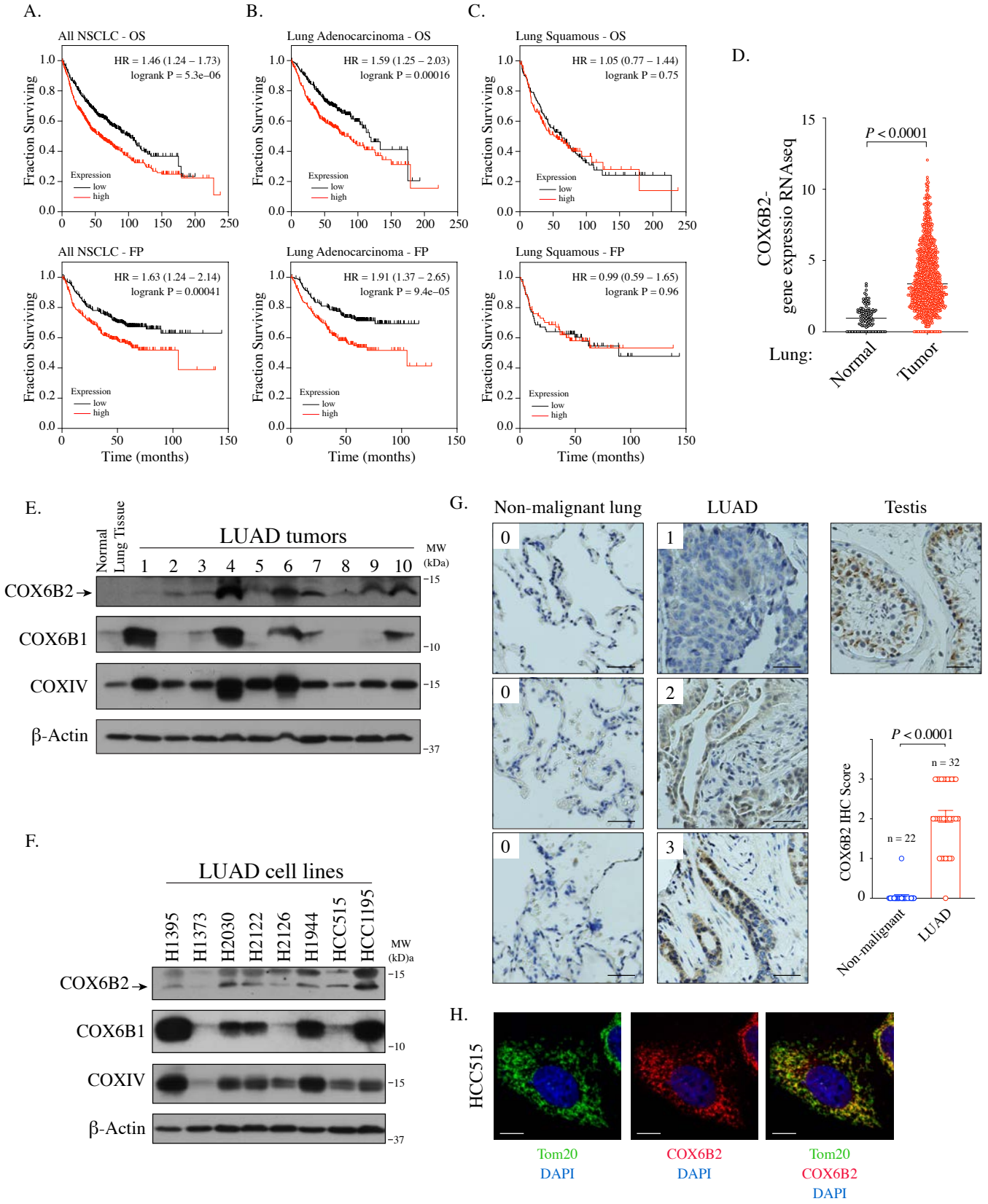

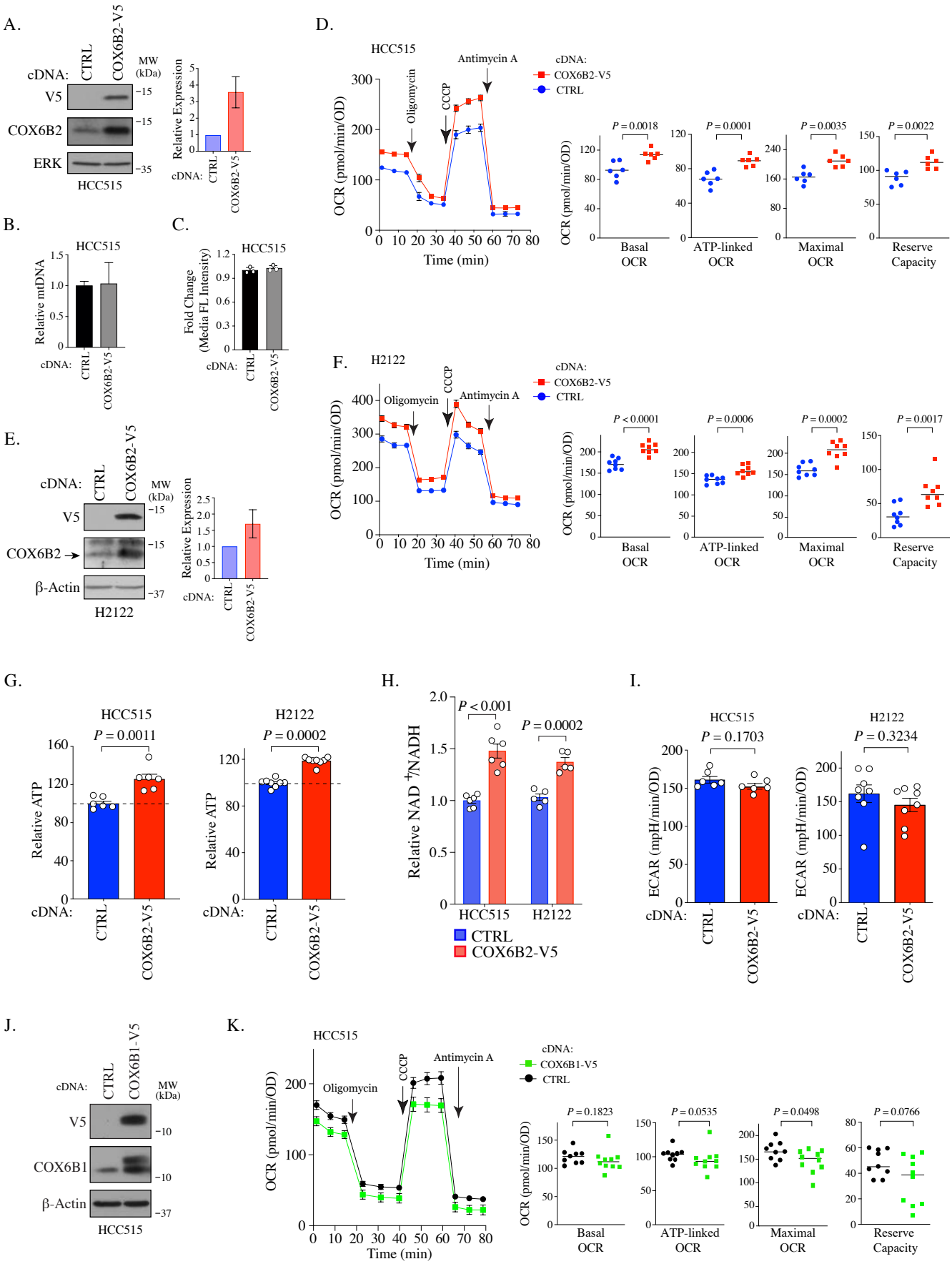
A.
cDNA: CTRL COX6B2-V5
MW (kDa)
V5
COX6B2
ERK
HCC515
Relative Expression
B.
HCC515
Relative mtDNA
C.
HCC515
Fold Change (Media FL Intensity)
D.
HCC515
Oligomycin
CCCP
Antimycin A
cDNA: COX6B2-V5 CTRL
OCR (pmol/min/OD)
Time (min)
P = 0.0018
P = 0.0001
P = 0.0035
P = 0.0022
Basal OCR
ATP-linked OCR
Maximal OCR
Reserve Capacity
E.
COX6B2
β-Actin
H2122
F.
H2122
P < 0.0001
P = 0.0006
P = 0.0002
P = 0.0017
G.
HCC515
P = 0.0011
H2122
P = 0.0002
Relative ATP
H.
P < 0.001
P = 0.0002
Relative NAD+/NADH
HCC515
H2122
CTRL
COX6B2-V5
I.
HCC515
P = 0.1703
H2122
P = 0.3234
ECAR (mpH/min/OD)
J.
COX6B1-V5
COX6B1
K.
COX6B1-V5
P = 0.1823
P = 0.0535
P = 0.0498
P = 0.0766

Cheng et al. Figure 3

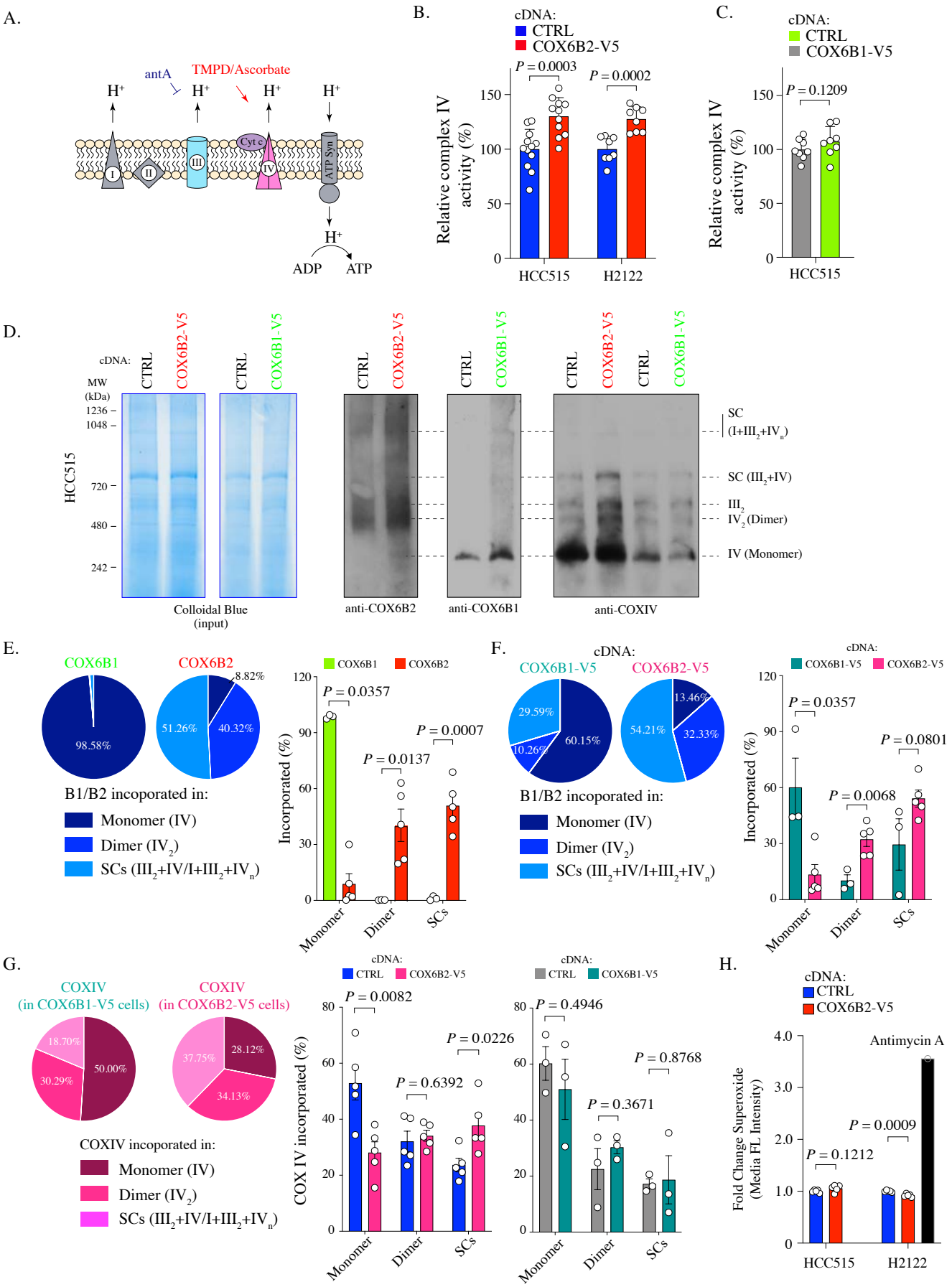

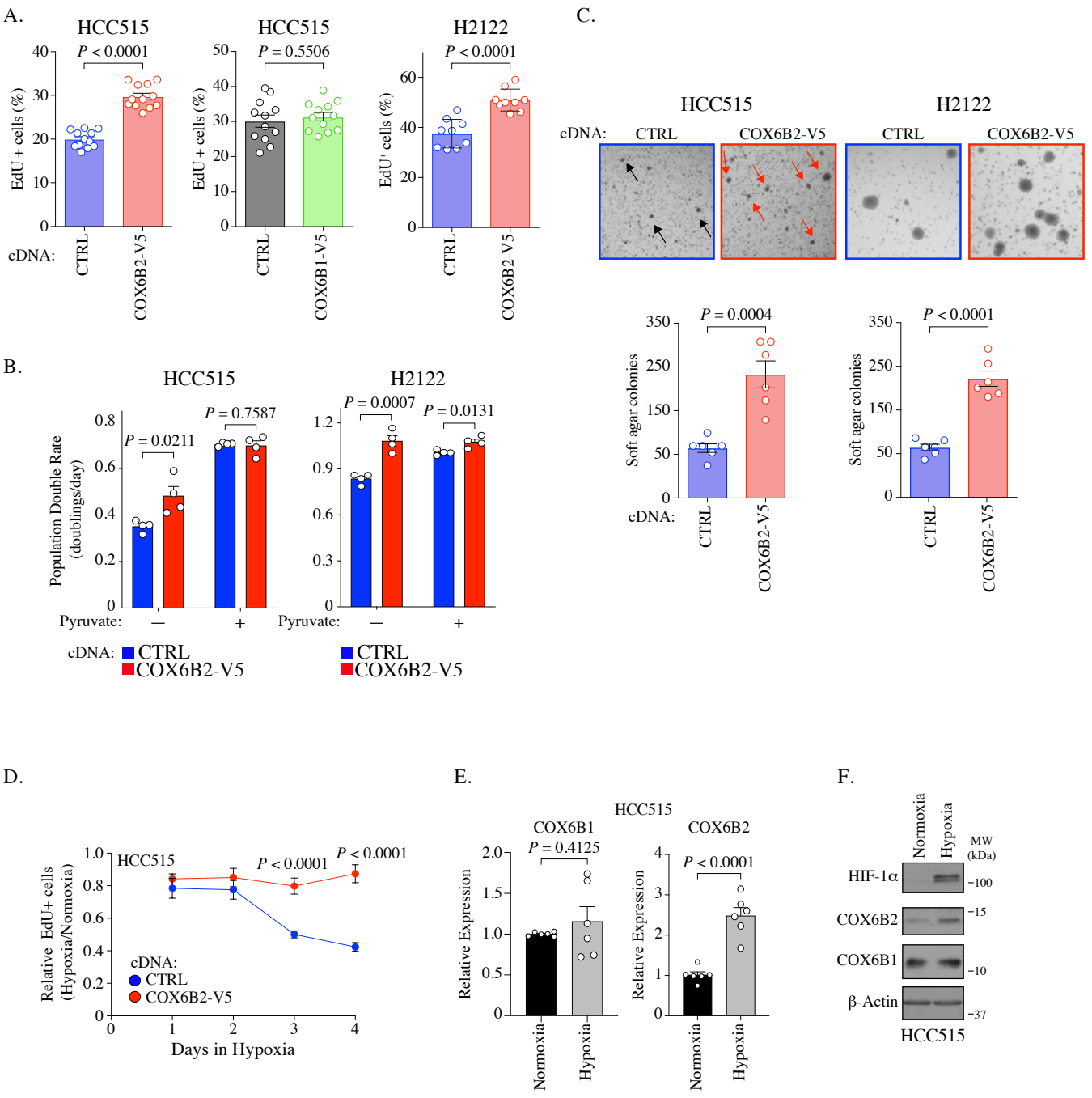
A.
HCC515
P < 0.0001
EdU + cells (%)
cDNA:
CTRL
COX6B2-V5
HCC515
P = 0.5506
EdU + cells (%)
CTRL
COX6B1-V5
H2122
P < 0.0001
EdU+ cells (%)
CTRL
COX6B2-V5
B.
HCC515
H2122
Population Double Rate (doublings/day)
P = 0.0211
P = 0.7587
P = 0.0007
P = 0.0131
Pyruvate: — +
cDNA: CTRL COX6B2-V5
C.
HCC515
H2122
cDNA: CTRL COX6B2-V5
Soft agar colonies
P = 0.0004
P < 0.0001
D.
HCC515
Relative EdU+ cells (Hypoxia/Normoxia)
P < 0.0001
P < 0.0001
cDNA:
CTRL
COX6B2-V5
Days in Hypoxia
E.
HCC515
COX6B1
P = 0.4125
COX6B2
P < 0.0001
Relative Expression
Normoxia
Hypoxia
F.
Normoxia
Hypoxia
MW (kDa)
HIF-1α
COX6B2
COX6B1
β-Actin
-100
-15
-10
-37
HCC515

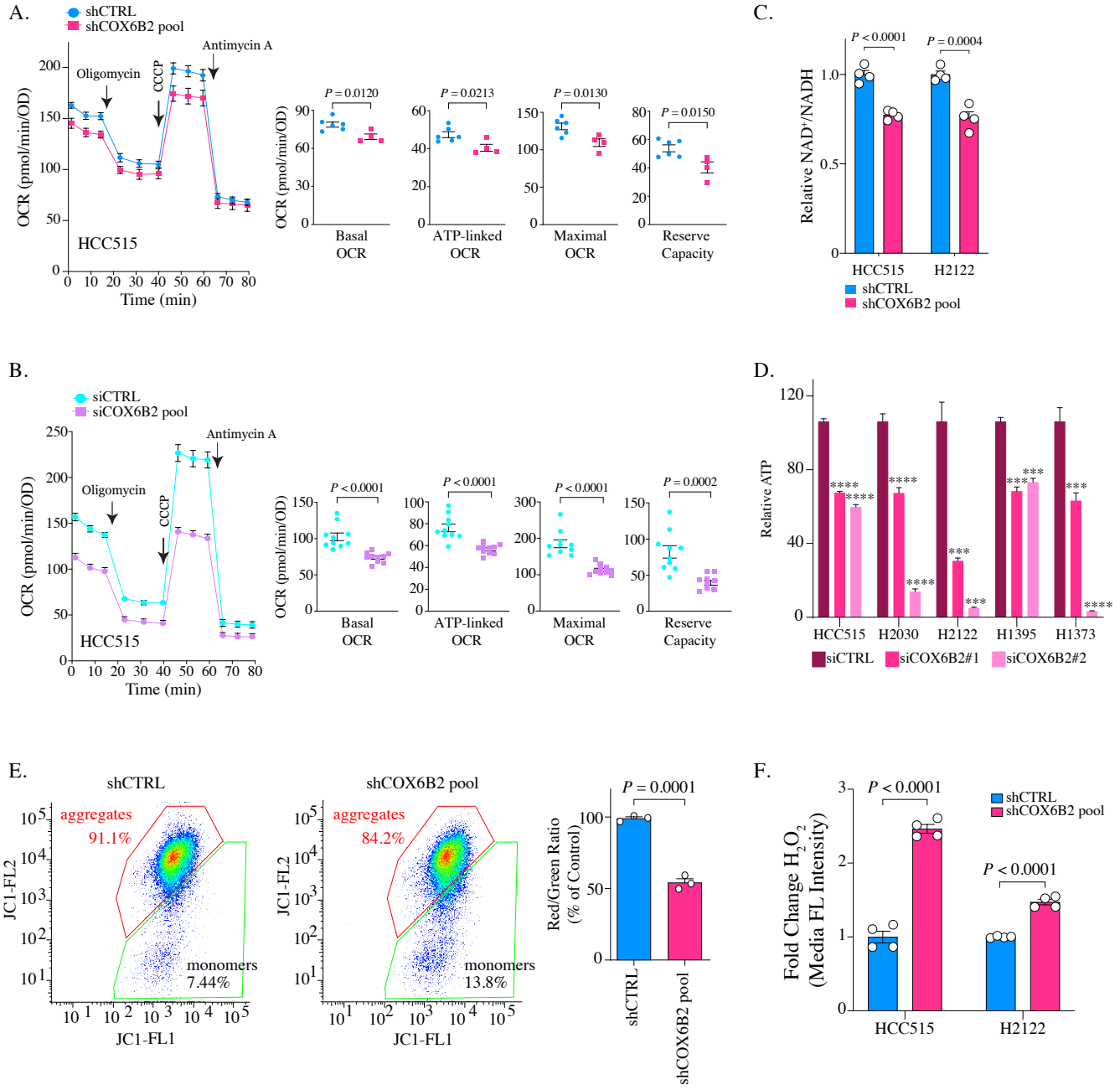
A.
shCTRL
shCOX6B2 pool
Oligomycin
CCCP
Antimycin A
OCR (pmol/min/OD)
HCC515
Time (min)
P = 0.0120
P = 0.0213
P = 0.0130
P = 0.0150
Basal OCR
ATP-linked OCR
Maximal OCR
Reserve Capacity
B.
siCTRL
siCOX6B2 pool
P < 0.0001
P < 0.0001
P < 0.0001
P = 0.0002
C.
P < 0.0001
P = 0.0004
Relative NAD+/NADH
HCC515
H2122
D.
Relative ATP
HCC515
H2030
H2122
H1395
H1373
siCTRL
siCOX6B2#1
siCOX6B2#2
E.
shCTRL
shCOX6B2 pool
aggregates
91.1%
monomers
7.44%
aggregates
84.2%
monomers
13.8%
JC1-FL1
JC1-FL2
P = 0.0001
Red/Green Ratio (% of Control)
F.
P < 0.0001
P < 0.0001
Fold Change H2O2 (Media FL Intensity)
HCC515
H2122

Cheng et al. Figure 6

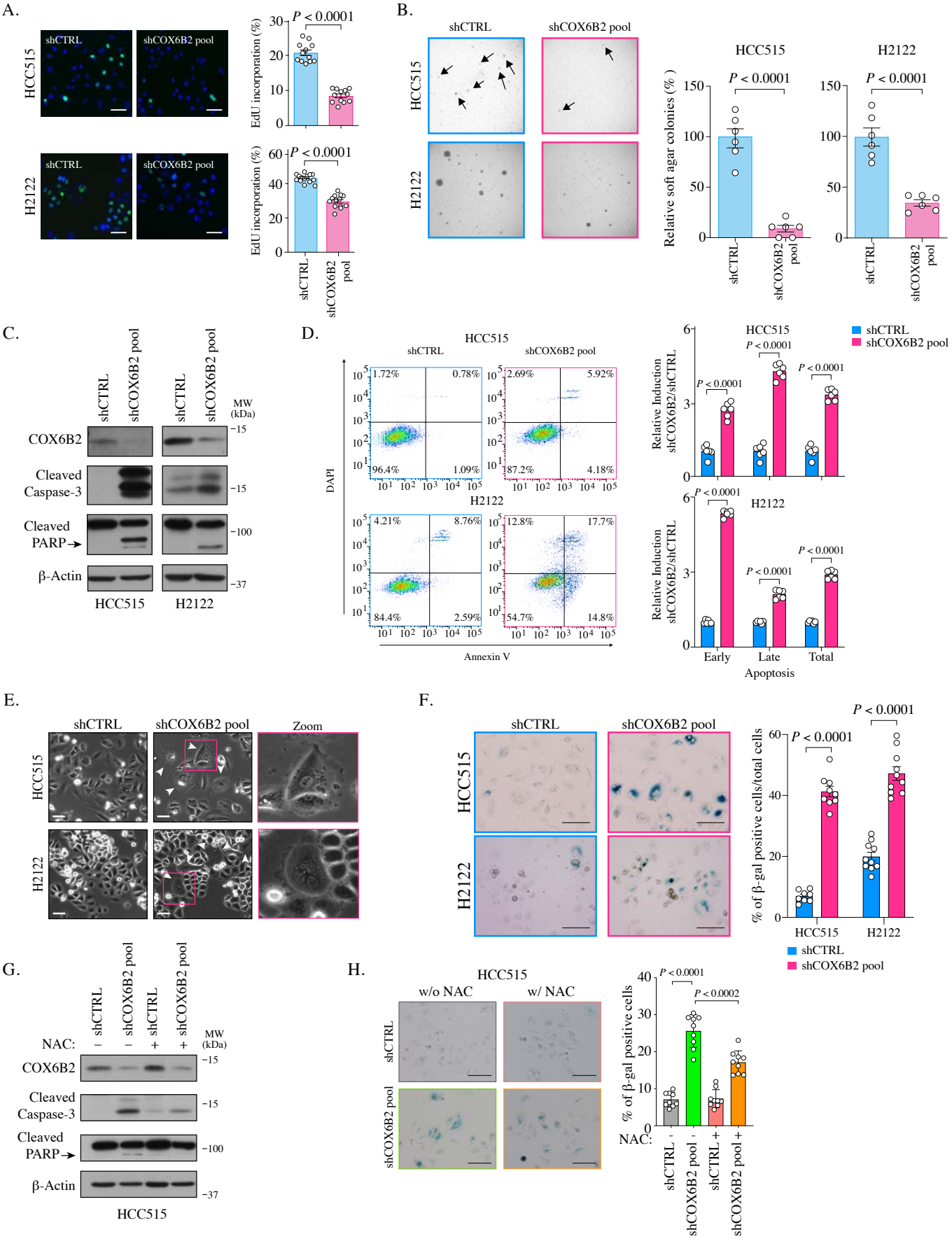
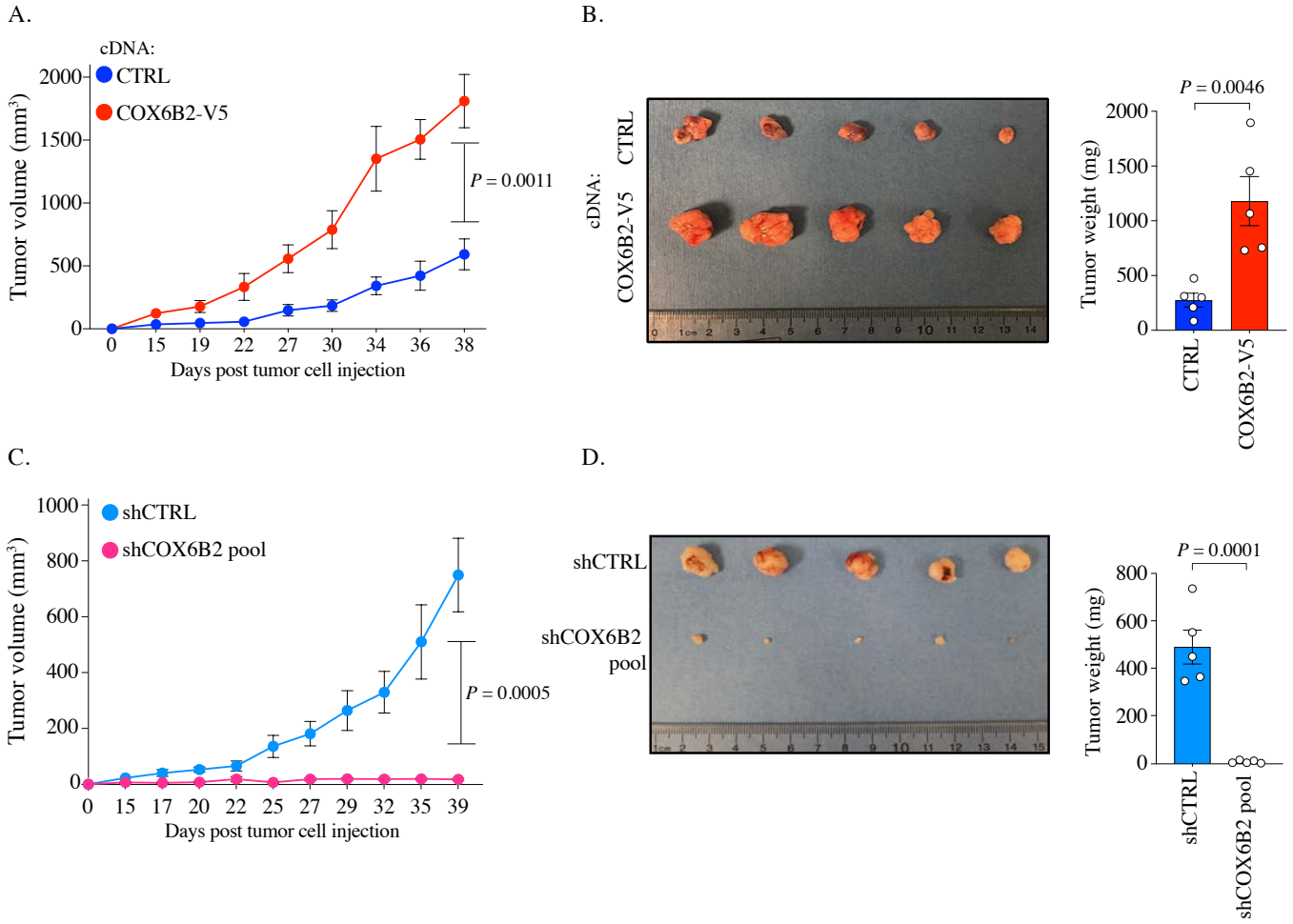
Cheng et al. Figure 7